Analytical Solution for the Internal Forces of the Nuclear Power Plant's Water Intake and Outlet Tunnel under P Waves

Yawei Duan, Lihua Wu, Dongyang Wang, Rongpeng Li and Di Jiang*

China Nuclear Power Engineering Co., Ltd., China National Nuclear Corporation, Beijing, China

INFORMATION

Keywords:
Water intake and outlet tunnel
analytical solutions
earthquake
internal forces
thick-walled cylinder
slippage effect

DOI: 10.23967/j.rimni.2026.10.78174

SCIPEDIA Revista Internacional de Métodos Numéricos para Cálculo y Diseño en Ingeniería

Revista Internacional Métodos numéricos para cálculo y diseño en ingeniería RIMNI

In cooperation with CIMNE

Analytical Solution for the Internal Forces of the Nuclear Power Plant's Water Intake and Outlet Tunnel under P Waves

Yawei Duan, Lihua Wu, Dongyang Wang, Rongpeng Li and Di Jiang*

China Nuclear Power Engineering Co., Ltd., China National Nuclear Corporation, Beijing, China

ABSTRACT

Analytical solutions provide an efficient means to evaluate the internal forces of tunnels and elucidate the relationships among key influencing parameters. This paper presents an analytical solution for the internal forces of the nuclear power plant's water intake and outlet tunnel under P waves. In order to consider the slippage effect of the ground-tunnel and lining-lining interfaces, a spring-type tangential stiffness coefficient K_i is introduced. Moreover, the proposed analytical solution can accommodate tunnels with an arbitrary number of lining layers and treat the linings as thick-walled cylinders, providing higher analytical accuracy. The validity of the proposed analytical solution is demonstrated through a comparative analysis with the traditional analytical solution and finite element simulations. The comparison results confirm the accuracy and superiority of the proposed method. A comprehensive parametric investigation is conducted to examine how the tangential stiffness coefficient K_i, the flexibility ratio F, and the characteristics of the isolation layer influence the tunnel's seismic behavior.

OPEN ACCESS

Received: 25/12/2025

Accepted: 28/01/2026

Published: 20/03/2026

DOI
10.23967/j.rimni.2026.10.78174

Keywords:
Water intake and outlet tunnel
analytical solutions
earthquake
internal forces
thick-walled cylinder
slippage effect

Nomenclature

n	Number of lining layers in the n-layer lining system
ρ	Radial coordinate in polar coordinates
φ	Polar angle
t_i	Thickness of the isolation layer
E_i, ν_i	Young's modulus and Poisson's ratio of the i-th lining layer
E_{n+1}, ν_{n+1}	Young's modulus and Poisson's ratio of the surrounding ground/rock
ρ_g, E_g, G	Mass density, Young's modulus, Shear modulus and Poisson's ratio of the ground/rock
K_i	Tangential spring stiffness coefficient at the i-th interface
K_s	Tangential spring stiffness used in FE contact implementation
K_{Nj}, K_{Tj}	Normal/tangential spring coefficients at boundary node j
$\mathbf{K_B}$, $\mathbf{C_B}$	Assembled stiffness and damping matrices of the viscous–spring boundary

*Correspondence: Di Jiang (jiangdicnpe@163.com).

u_ρ, u_φ	Radial displacement, Circumferential displacement
σ_ρ, σ_φ, $\tau_{\rho\varphi}$	Radial normal stress, Circumferential normal stress, Shear stress
T_{max}, M_{max}	Absolute maximum thrust and moment during the entire earthquake loading history
A, B, C, D	Undetermined constants in the general solution of axisymmetric stress functions
I, J	Undetermined constants in separation
W, F, G, H	Undetermined constants in the general solution under shear stresses
t	Time
$\sigma_v(t)$, $\sigma_h(t)$	Vertical and Horizontal far-field normal stress
c_p, c_s	P wave and S-wave velocity of the ground
$v(t)$	Seismic wave particle velocity time history
p, τ	Hydrostatic pressure component and Pure shear stress component

1 Introduction

As an important clean energy source for optimizing the energy structure, nuclear power has become an essential option for actively and prudently promoting carbon peaking and carbon neutrality. At present, most nuclear power plants in China are located in coastal areas and generally adopt once-through cooling systems that use seawater as the cooling medium. The cooling water and safety-related water are conveyed through an intake tunnel to the PX pump house, and then discharged through an outlet tunnel. According to the Standard for Seismic Design of Nuclear Power Plants (GB 50267-2019) [1] and the Structural Design Code for the Tunnels of Water Intake and Outlet for Nuclear Power Plants (NB/T 20389-2016) [2], the safety-related intake and outlet tunnels of nuclear power plants are classified as Seismic Category I structures. Ensuring their safety and reliability during earthquakes is therefore crucial to the safe operation of nuclear power plants. Traditionally, it has been believed that tunnels, being constrained by the surrounding soil and rock mass, exhibit better seismic performance than surface structures. However, during major earthquakes over the past few decades [3–5], numerous tunnels and underground structures have suffered varying degrees of seismic damage, including lining cracking, dislocation, deformation, and even collapse. Therefore, earthquakes pose a significant threat to the safety of water intake and outlet tunnels in nuclear power plants. The issue of tunnel seismic resistance should not be neglected, and conducting seismic analysis and research on tunnel structures is of great engineering significance.

At present, the seismic analysis methods of tunnels can generally be categorized into analytical solutions, the quasi-static method, and the dynamic time-history method [6]. Compared with the quasi-static analysis solutions and dynamic time history analysis method, although the analytical solution is based on certain assumptions, the internal forces of the tunnel under seismic loading can be obtained simply and quickly, and clarify the correlations among key influencing parameters. Therefore, this method has been extensively adopted in the preliminary seismic design of tunnels. Numerous scholars have derived analytical solutions for evaluating the internal forces and deformations of tunnels under seismic loading by assuming that the contact conditions between the tunnel and the ground are no-slip and full-slip [7–10]. To further investigate the influence of interface behavior and lining rigidity, Basirat et al. [11] systematically compared the seismic response of monolithic and segmental tunnel linings under full-slip and no-slip interface conditions using analytical methods, a quasi-static approach, and numerical simulation. The results demonstrated that no-slip conditions significantly amplify lining stresses, while segmental linings exhibit lower stresses but larger strains due to the reduced stiffness introduced by joints, highlighting the critical role of interface behavior and lining stiffness in tunnel seismic performance. In fact, the actual contact condition lies between these two idealized states. To account for the slippage effect, Park et al. [12] introduced a spring-based flexibility

coefficient D, enabling a more realistic analytical solution for circular tunnels under seismic loading. Most existing analytical models assume that the surrounding ground is dry soil without considering the pore water pressure. To address this limitation, Bobet [13] proposed an analytical approach that considers both seismic and static load while incorporating the effect of pore pressure. In addition, traditional analytical solutions typically idealize the tunnel lining as a beam or shell element, which may induce considerable inaccuracies for thick linings [14,15]. To mitigate this issue, Huang et al. [16] modeled the tunnel as a thick-walled cylinder and established an analytical solution for circular tunnels subjected to obliquely incident SV waves, significantly improving the predictive accuracy of the analytical solution. For common composite tunnels, some scholars have proposed analytical solutions for the internal forces and displacements of the composite tunnel under seismic induced shear stresses [17,18].

It is worth noting that the above-mentioned analytical solutions can only address the response under SV wave excitation. However, many studies have shown that P waves significantly affect the seismic response of tunnels [19–22], and the Standard for Seismic Design of Nuclear Power Plants (GB 50267-2019) [1] clearly stipulates that the seismic action should be calculated in two orthogonal horizontal directions (SV waves) and one vertical direction (P waves). Recently, Basirat [23] extended the work of Einstein and Schwartz (1979) by proposing an analytical method for calculating tunnel lining internal forces under P waves in both no-slip and full-slip conditions. In addition, the effects of P waves and S-waves on lining internal forces were compared through analytical solutions and numerical analysis, providing a more detailed understanding of the seismic behavior of tunnels. Building upon these studies, existing analytical solutions for P wave excitation have mainly been established for single-layer tunnel linings. In practical nuclear power engineering, intake and outlet tunnels are commonly constructed using double-lining or composite lining systems (such as a shield lining combined with a secondary lining). Especially as high-quality bedrock sites become increasingly scarce, the application of composite-lined tunnels is expected to become more widespread in order to cope with complex geological conditions. However, an analytical solution for composite tunnels in nuclear power engineering under P wave excitation remains vacant.

This paper presents an analytical solution for predicting the thrust and moment of intake and outlet tunnels in nuclear power plants with an arbitrary number of lining layers under P waves. The tunnel lining is regarded as a thick-walled cylinder, which mitigates the inaccuracies of conventional analytical solutions for thick linings. The tangential stiffness coefficient K_i is introduced to consider the slippage effect at the interface of ground-tunnel and lining-lining. Then, the thrust and moment predicted by the proposed analytical solution are compared with the dynamic time history analysis method results. Finally, the effects of tangential stiffness coefficient K_i, flexibility ratio F, isolation layer and steel plate are investigated.

2 Definition of the Problem

Consider a water intake and outlet tunnel of a nuclear power plant with an n-layer lining system subjected to vertically incident P waves propagating across the tunnel cross-section. The tunnel is assumed to be located at the origin O of the X-Y coordinate system. For the i-th lining layer ($i = 1, 2, \ldots, n$), the inner and outer radii are denoted by r_{i-1}, r_i, while the corresponding Young's modulus and Poisson's ratio are represented by E_i, ν_i, respectively. The mechanical properties of the surrounding ground are described by the Young's modulus E_{n+1}, Poisson's ratio ν_{n+1}, and mass density ρ_g.

The following assumptions are made for this problem: (1) the lining and surrounding ground are homogeneous, isotropic, and linearly elastic materials; (2) the tunnel is deeply embedded, typically at

a depth greater than twice its radius; (3) the wavelength corresponding to the predominant frequency of the seismic wave is significantly greater than the diameter of the tunnel.

A vertically incident plane P wave is essentially a body wave, whose propagation primarily induces cyclic compression and extension of the soil medium along the direction of wave travel, thereby generating a time-varying normal stress state in the free field. Since the predominant wavelength of seismic waves is generally much larger than the characteristic cross-sectional dimensions of typical underground structures, the spatial variation of free-field stresses and strains can be reasonably regarded as negligible at the scale of the tunnel cross-section.

Under this long-wavelength assumption, the seismic action induced by a vertically incident P wave in the free field can be equivalently represented as a spatially uniform far-field normal stress state acting on the surrounding ground, consisting of the vertical stress $\sigma_v(t)$ along the direction of wave propagation and the accompanying horizontal stress $\sigma_h(t)$, which arises from the elastic constitutive relationship and the plane-strain constraint, as shown in Fig. 1. The explicit expressions of $\sigma_v(t)$ and $\sigma_h(t)$ are given in Eq. (1). Consequently, at any time instant t, the dynamic response of the tunnel-ground system can be simplified to a pseudo-static problem under two-dimensional plane-strain conditions, in which spatially uniform but time-dependent far-field stresses are applied to the tunnel cross-section. This equivalence approach essentially transforms the dynamic free-field stress state induced by the incident P wave into a quasi-static boundary loading applied at each time instant. Similar pseudo-static treatments have been extensively employed in the derivation of analytical solutions for tunnels subjected to P wave excitation [13,23,24] and are supported by clear physical interpretations and sound engineering justification.

$$\begin{cases} \sigma_v(t) = \dfrac{E_{n+1}(1-\upsilon_{n+1})}{(1+\upsilon_{n+1})(1-2\upsilon_{n+1})c_p} v(t) \\ \sigma_h(t) = \dfrac{E_{n+1}\upsilon_{n+1}}{(1+\upsilon_{n+1})(1-2\upsilon_{n+1})c_p} v(t) \end{cases} \tag{1}$$

where c_p is the P waves velocity of the ground and $v(t)$ is the seismic wave velocity time history.

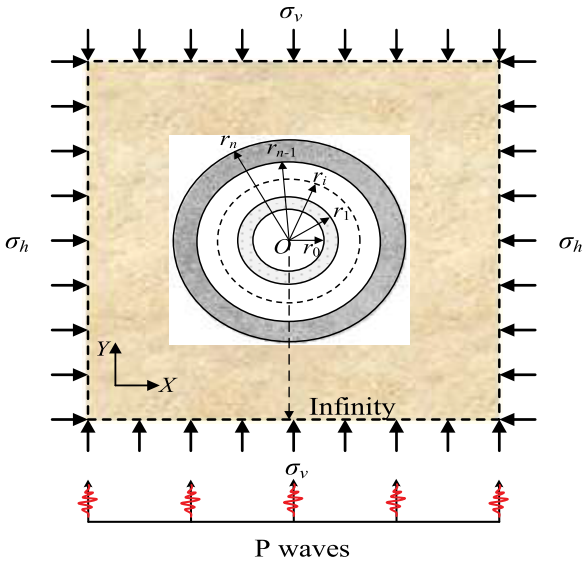

Figure 1: The pseudo-static analysis model of the ground-tunnel system under P waves

The far-field stress induced by P waves can be decomposed into two independent components: a hydrostatic pressure p and a pure shear stress τ, as illustrated in Fig. 2. The corresponding expressions for p and τ are given as follows

$$\begin{cases} p = \dfrac{\sigma_v + \sigma_h}{2} \\ \tau = \dfrac{\sigma_v - \sigma_h}{2} \end{cases} \tag{2}$$

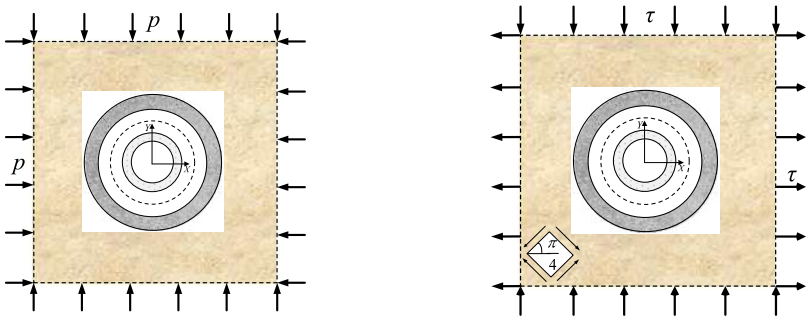

Figure 2: Stress decomposition in the pseudo-static model under P wave excitation: (a) hydrostatic pressure p; (b) pure shear stress τ

3 Derivation of the Analytical Solution

In this section, analytical solutions for the internal forces of the nuclear power plant's intake and outlet tunnels under P wave excitation are derived. The far-field stress generated by P wave incidence is decomposed into two components: a hydrostatic pressure and a pure shear stress. Accordingly, the governing equations of the ground-tunnel system corresponding to these two components are established separately, and the analytical solution is obtained by solving all equations simultaneously. Butscher [25] and Huang et al. [16] indicate that when the thickness-to-radius ratio is greater than 0.1, the error of traditional analytical solutions that idealize the lining as a beam or shell model exceeds 10%. Therefore, different from the widely used analytical solution [7,9,13], the tunnel lining is regarded as a thick-walled cylinder in this study to solve the error caused by the thick lining.

3.1 Equations for Hydrostatic Pressure Component

As illustrated in Fig. 2a, the ground-tunnel system is initially defined in the Cartesian coordinate system (X-Y) and then transformed into the polar coordinate system (ρ-φ), as shown in Fig. 3a. For analytical convenience, the tunnel subjected to hydrostatic pressure (Fig. 3a) can be decomposed into the following components: (1) a cylindrical cavity subjected to an outward internal pressure p_n and inward external pressure p (Fig. 3b); (2) n thick-walled cylinders, wherein the internal pressure of the i-th thick-walled cylinder is p_{i-1}, and the external pressure is p_i. In particular, the inner surface of the first layer of lining is free (Fig. 3c).

The plane strain problem formulated in polar coordinates, as shown in Fig. 3, is solved using the classical stress function approach. The analytical solution is required to satisfy the compatibility relation, prescribed boundary conditions, and the continuity of both displacement and stress across

all interfaces. The detailed derivation of the governing equations required for the model subjected to hydrostatic pressure is provided in Appendix A. The Eqs. (A12)–(A14) and (A17) are necessary for solving the solution for the water intake and outlet tunnel under hydrostatic pressure.

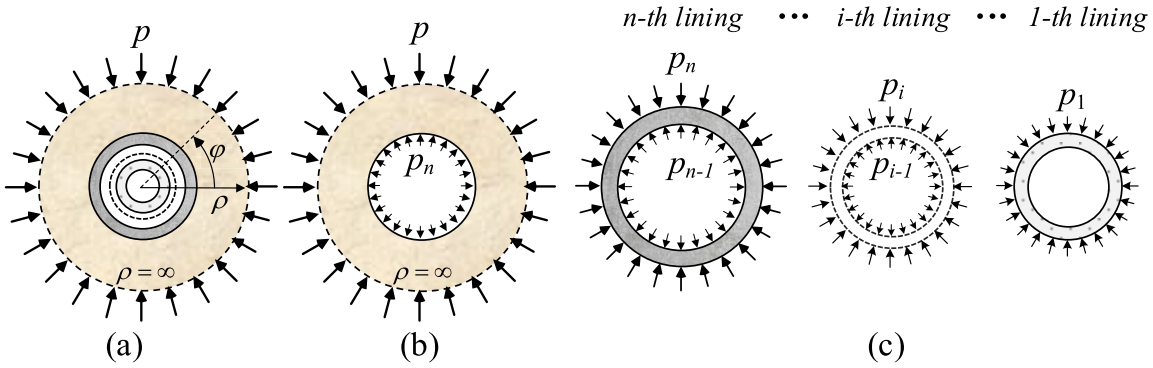

Figure 3: Decomposition of system under hydrostatic pressure: (a) ground-lining; (b) ground; (c) n lining layers

3.2 Equations for Pure Shear Stress Component

The ground-tunnel system under shear stress, as illustrated in Fig. 2b, is transformed from the Cartesian coordinate system (X-Y) into the polar coordinate system (ρ-φ), as shown in Fig. 4a. The far-field stress in polar coordinates is given by Eq. (3). Similar to Section 3.1, the system under shear stress can be divided into two parts: (1) a cylindrical cavity (ground) loaded with the far-field external radial stress $\tau\cos 2\varphi$ and circumferential stress $-\tau\sin 2\varphi$, where the stress amplitude τ is determined according to Eq. (2). In addition, $p_n\cos 2\varphi$ and $q_n\sin 2\varphi$ are defined as the radial and circumferential reaction stresses exerted by the outermost lining on the inner surface of the cylindrical cavity. (Fig. 4b); (2) n thick-walled cylinders, of which the i-th thick-walled cylinder is subjected to radial reaction stress $p_i\cos 2\varphi$ and circumferential reaction stress $q_i\sin 2\varphi$ exerted by the $(i+1)$-th lining layer on its outer surface, and radial reaction stress $p_{i-1}\cos 2\varphi$ and circumferential reaction stress $q_{i-1}\sin 2\varphi$ exerted by the $(i-1)$-th lining layer on its inner surface. Specially, the inner boundary of the first lining is assumed to be free, as illustrated in Fig. 4c.

$$\begin{cases} \sigma_\rho\big|_{\rho=\infty} = \tau\cos 2\varphi \\ \tau_{\rho\varphi}\big|_{\rho=\infty} = -\tau\sin 2\varphi \end{cases} \tag{3}$$

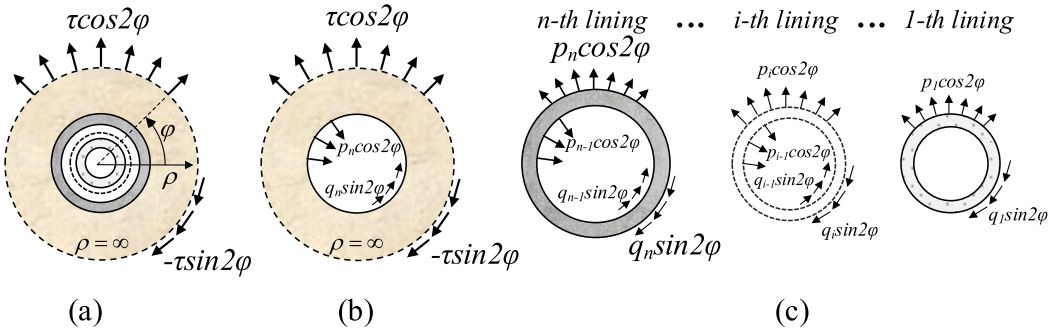

Figure 4: Decomposition of system under shear stress: (a) ground-lining; (b) ground; (c) n lining layers

To account for the slippage behavior at every interface, a tangential spring stiffness coefficient K_i is introduced, following the approach proposed by Park et al. [12]. Two idealized cases $K_i \to 0$ and $K_i \to \infty$, correspond to the full-slip and no-slip (perfectly bonded) interface contact conditions, respectively. Therefore, the continuity of displacement at the interface $\rho = r_i$ can be given by

$$\begin{cases} u_{\rho(i)}\big|_{\rho=r_i} = u_{\rho(i+1)}\big|_{\rho=r_i} \\ u_{\varphi(i)}\big|_{\rho=r_i} = u_{\varphi(i+1)}\big|_{\rho=r_i} + q_i \sin 2\varphi / K_i \end{cases} \tag{4}$$

At the interface $\rho = r_i$, stress continuity conditions must be satisfied

$$\begin{cases} \tau_{\rho\phi(i)}\big|_{\rho=r_i} = \tau_{\rho\phi(i+1)}\big|_{\rho=r_i} \\ \sigma_{\rho(i)}\big|_{\rho=r_i} = \sigma_{\rho(i+1)}\big|_{\rho=r_i} \end{cases} \tag{5}$$

The plane strain problem formulated in polar coordinates, as shown in Fig. 4, is solved using the classical stress function approach. The detailed derivation of the governing equations required for the model subjected to shear stress is provided in Appendix B. The Eqs. (A31), (A33), (A37) and (A38) given above are necessary for solving the analytical solution for the composite tunnel under pure shear stress.

3.3 Present Analytical Solutions

Combining Eqs. (A12)–(A14), (A17), (A31), (A32), (A37) and (A38), the resulting matrix equation can be written in the following form

$$\mathbf{E}\,[6n+6, 6n+6] \cdot \begin{bmatrix} A_1 \\ C_1 \\ W_1 \\ F_1 \\ G_1 \\ H_1 \\ \cdot \\ \cdot \\ \cdot \\ A_{n+1} \\ C_{n+1} \\ W_{n+1} \\ F_{n+1} \\ G_{n+1} \\ H_{n+1} \end{bmatrix} = \begin{bmatrix} 0 \\ 0 \\ 0 \\ 0 \\ 0 \\ 0 \\ \cdot \\ \cdot \\ \cdot \\ 0 \\ 0 \\ 0 \\ -\dfrac{p}{2} \\ 0 \\ -\dfrac{\tau}{2} \end{bmatrix} \tag{6}$$

where $\mathbf{E}$ is a $(6n+6) \times (6n+6)$ matrix, the elements of which are defined as follows

$$\begin{bmatrix} E_{1,1} & E_{1,2} & E_{1,3} & E_{1,4} & E_{1,5} & E_{1,6} \\ E_{2,1} & E_{2,2} & E_{2,3} & E_{2,4} & E_{2,5} & E_{2,6} \\ E_{3,1} & E_{3,2} & E_{3,3} & E_{3,4} & E_{3,5} & E_{3,6} \end{bmatrix} = \begin{bmatrix} \dfrac{1}{r_0^2} & 2 & 0 & 0 & 0 & 0 \\ 0 & 0 & 6r_0{}^2 & 2 & -\dfrac{2}{r_0{}^2} & -\dfrac{6}{r_0{}^4} \\ 0 & 0 & 0 & 2 & \dfrac{4}{r_0{}^2} & \dfrac{6}{r_0{}^4} \end{bmatrix}$$

$$\begin{bmatrix} E_{6i-2,6i-5} & E_{6i-2,6i-4} & E_{6i-2,6i-3} & E_{6i-2,6i-2} & E_{6i-2,6i-1} & E_{6i-2,6i} \\ E_{6i-1,6i-5} & E_{6i-2,6i-4} & E_{6i-2,6i-3} & E_{6i-2,6i-2} & E_{6i-2,6i-1} & E_{6i-2,6i} \\ E_{6i,6i-5} & E_{6i-2,6i-4} & E_{6i-2,6i-3} & E_{6i-2,6i-2} & E_{6i-2,6i-1} & E_{6i-2,6i} \\ E_{6i+1,6i-5} & E_{6i-2,6i-4} & E_{6i-2,6i-3} & E_{6i-2,6i-2} & E_{6i-2,6i-1} & E_{6i-2,6i} \\ E_{6i+2,6i-5} & E_{6i-2,6i-4} & E_{6i-2,6i-3} & E_{6i-2,6i-2} & E_{6i-2,6i-1} & E_{6i-2,6i} \\ E_{6i+3,6i-5} & E_{6i-2,6i-4} & E_{6i-2,6i-3} & E_{6i-2,6i-2} & E_{6i-2,6i-1} & E_{6i-2,6i} \end{bmatrix} =$$

$$\begin{bmatrix} \frac{1}{r_i^2} & 2 & 0 & 0 & 0 & 0 \\ \frac{k_{2(i)}-k_{1(i)}}{r_i} & 2\left(k_{1(i)}+k_{2(i)}\right)r_i & 0 & 0 & 0 & 0 \\ 0 & 0 & 6{r_i}^2 & 2 & -\frac{2}{{r_i}^2} & -\frac{6}{{r_i}^4} \\ 0 & 0 & 0 & 2 & \frac{4}{{r_i}^2} & \frac{6}{{r_i}^4} \\ 0 & 0 & 4k_{2(i)}{r_i}^3 & 2\left(k_{2(i)}-k_{1(i)}\right)r_i & \frac{4k_{1(i)}}{r_i} & 2\frac{k_{1(i)}-k_{2(i)}}{{r_i}^3} \\ 0 & 0 & \left(2k_{2(i)}-6k_{1(i)}\right){r_i}^3-6{r_i}^2/K_i & 2\left(k_{2(i)}-k_{1(i)}\right)r_i-2/K_i & 2\frac{k_{1(i)}+k_{2(i)}}{r_i}+\frac{2}{{r_i}^2K_i} & 2\frac{k_{2(i)}-k_{1(i)}}{{r_i}^3}+\frac{6}{{r_i}^4K_i} \end{bmatrix}$$

$$\begin{bmatrix} E_{6i-2,6i+1} & E_{6i-2,6i+2} & E_{6i-2,6i+3} & E_{6i-2,6i+4} & E_{6i-2,6i+5} & E_{6i-2,6i+6} \\ E_{6i-1,6i+1} & E_{6i-2,6i+2} & E_{6i-2,6i+3} & E_{6i-2,6i+4} & E_{6i-2,6i+5} & E_{6i-2,6i+6} \\ E_{6i,6i+1} & E_{6i-2,6i+2} & E_{6i-2,6i+3} & E_{6i-2,6i+4} & E_{6i-2,6i+5} & E_{6i-2,6i+6} \\ E_{6i+1,6i+1} & E_{6i-2,6i+2} & E_{6i-2,6i+3} & E_{6i-2,6i+4} & E_{6i-2,6i+5} & E_{6i-2,6i+6} \\ E_{6i+2,6i+1} & E_{6i-2,6i+2} & E_{6i-2,6i+3} & E_{6i-2,6i+4} & E_{6i-2,6i+5} & E_{6i-2,6i+6} \\ E_{6i+3,6i+1} & E_{6i-2,6i+2} & E_{6i-2,6i+3} & E_{6i-2,6i+4} & E_{6i-2,6i+5} & E_{6i-2,6i+6} \end{bmatrix} =$$

$$\begin{bmatrix} -\frac{1}{r_i^2} & -2 & 0 & 0 & 0 & 0 \\ \frac{k_{1(i+1)}-k_{2(i+1)}}{r_i} & -2\left(k_{1(i+1)}+k_{2(i+1)}\right)r_i & 0 & 0 & 0 & 0 \\ 0 & 0 & -6{r_i}^2 & -2 & \frac{2}{{r_i}^2} & \frac{6}{{r_i}^4} \\ 0 & 0 & 0 & -2 & -\frac{4}{{r_i}^2} & -\frac{6}{{r_i}^4} \\ 0 & 0 & -4k_{2(i+1)}{r_i}^3 & 2\left(k_{1(i+1)}-k_{2(i+1)}\right)r_i & -\frac{4k_{1(i+1)}}{r_i} & 2\frac{k_{2(i+1)}-k_{1(i+1)}}{{r_i}^3} \\ 0 & 0 & \left(6k_{1(i+1)}-2k_{2(i+1)}\right){r_i}^3 & 2\left(k_{1(i+1)}-k_{2(i+1)}\right)r_i & -2\frac{k_{1(i+1)}+k_{2(i+1)}}{r_i} & 2\frac{k_{1(i+1)}-k_{2(i+1)}}{{r_i}^3} \end{bmatrix}$$

$E_{6n+4,6n+2} = E_{6n+5,6n+3} = E_{6n+6,6n+4} = 1$, and other elements are 0.

By solving Eq. (10), the expressions of A_i, C_i, W_i, F_i, G_i, H_i can be obtained. By substituting A_i, C_i and W_i, F_i, G_i, H_i into Eqs. (A5) and (A22), respectively, yields the stress components of the i-th lining corresponding to the hydrostatic pressure and pure shear stress components.

For the i-th lining segment, the thrust and moment are derived through the integration of the tangential stress, as follows

$$\begin{cases} T_i = \int_{r_{i-1}}^{r_i} \sigma_{\varphi(i)} dp \\ M_i = \int_{r_{i-1}}^{r_i} \sigma_{\varphi(i)} d(\rho - \frac{r_i + r_{i-1}}{2}) dp \end{cases} \tag{7}$$

Substituting Eqs. (A5) and (A22) into Eq. (7), the analytical solution for thrust and moment of intake and outlet tunnels in nuclear power plants with an arbitrary number of lining layers under P waves is

$$\begin{cases} T_i = A_i\left(r_i^{-1} - r_{i-1}^{-1}\right) + 2C_i\left(r_i - r_{i-1}\right) + \left[4W_i\left(r_i^{3} - r_{i-1}^{3}\right) + 2F_i\left(r_i - r_{i-1}\right) - 2H_i\left(r_i^{-3} - r_{i-1}^{-3}\right)\right]\cos 2\varphi \\ M_i = C_i\left(r_i^{2} - r_{i-1}^{2}\right) - A_i \ln\left(r_i / r_{i-1}\right) + \left[3W_i\left(r_i^{4} - r_{i-1}^{4}\right) + F_i\left(r_i^{2} - r_{i-1}^{2}\right) - 3H_i\left(r_i^{-2} - r_{i-1}^{-2}\right)\right]\cos 2\varphi - \dfrac{r_i + r_{i-1}}{2} T_i \end{cases} \tag{8}$$

3.4 Analytical Expression for Tunnels with Single Lining

Given the high complexity of the analytical expression for the seismic response of tunnels with multi-layer linings, this section will give an analytical expression for tunnels with a single lining. When $n = 1$, it indicates that the intake and outlet tunnels of the nuclear power plant have a single lining. Substituting $n = 1$ into Eq. (6) and solving, the explicit expression of A_1, C_1, E_1, F_1, G_1, H_1 is given by

$$\begin{cases} A_1 = \dfrac{2k_{1(2)}r_1^{2}}{k_{1(1)}\left(1+\xi^{2}\right) - \left(k_{1(2)} + k_{2(1)} - k_{2(2)}\right)\left(1-\xi^{2}\right)} p \\ C_1 = \dfrac{k_{1(2)}}{k_{1(1)}\left(1+\xi^{-2}\right) - \left(k_{1(2)} + k_{2(1)} - k_{2(2)}\right)\left(\xi^{-2}-1\right)} p \\ W_1 = -\dfrac{\xi^{4}(m-n) + 3\xi^{2}(m+n)}{6\left(\xi^{2}-1\right)^{3} {r_0}^{2}} \tau \\ F_1 = \dfrac{\left(\xi^{6} + \xi^{4} + 2\xi^{2}\right)m + 2\xi^{2} n}{2\left(\xi^{2}-1\right)^{3}} \tau \\ G_1 = -\dfrac{{r_1}^{2}\left[2\xi^{4} m + \left(\xi^{2}+1\right)(m+n)\right]}{2\left(\xi^{2}-1\right)^{3}} \tau \\ H_1 = \dfrac{{r_0}^{4}\left(3\xi^{6} m + \xi^{4} m + 2\xi^{4} n\right)}{6\left(\xi^{2}-1\right)^{3}} \tau \end{cases} \tag{9}$$

in which

$$\begin{cases} m = \dfrac{-4k_{1(2)}r_1\left(\dfrac{k_{1(2)} - k_{2(2)}}{3} r_1 + \alpha_2 + \alpha_3 + K_1\right)}{\left(\dfrac{4k_{1(2)} + 2k_{2(2)}}{3} r_1 - \alpha_2\right)\left(\dfrac{k_{1(2)} - k_{2(2)}}{3} r_1 + \alpha_2 + \alpha_3 + K_1\right) + \left(\dfrac{k_{1(2)} - k_{2(2)}}{3} r_1 - \alpha_1 + \alpha_2\right)\left(\dfrac{5k_{1(2)} + k_{2(2)}}{3} r_1 + \alpha_3 + K_1\right)} \\ n = \dfrac{-4k_{1(2)}r_1\left(\dfrac{k_{1(2)} - k_{2(2)}}{3} r_1 - \alpha_{11} + \alpha_{12}\right)}{\left(\dfrac{4k_{1(2)} + 2k_{2(2)}}{3} r_1 - \alpha_2\right)\left(\dfrac{k_{1(2)} - k_{2(2)}}{3} r_1 + \alpha_2 + \alpha_3 + K_1\right) + \left(\dfrac{k_{1(2)} - k_{2(2)}}{3} r_1 - \alpha_1 + \alpha_2\right)\left(\dfrac{5k_{1(2)} + k_{2(2)}}{3} r_1 + \alpha_3 + K_1\right)} \\ \xi = \dfrac{r_1}{r_0} \end{cases}$$

where,

$$\begin{cases} \alpha_1 = 2r_0 \dfrac{\left(k_{2(1)} - 3k_{1(1)}\right)\left(\xi^{7} + 3\xi^{3}\right) - \left(k_{2(1)} + 5k_{1(1)}\right)\left(3\xi^{5} + \xi\right)}{6\left(\xi^{2}-1\right)^{3}} \\ \alpha_2 = 4r_0 \dfrac{k_{2(1)}\xi^{7} - 3k_{2(1)}\xi^{5} + 3\left(k_{2(1)} - 2k_{1(1)}\right)\xi^{3} - \left(k_{2(1)} + 2k_{1(1)}\right)\xi}{6\left(\xi^{2}-1\right)^{3}} \\ \alpha_3 = 2r_0 \dfrac{\left(3k_{1(1)} - k_{2(1)}\right)\left(\xi^{7} - 3\xi^{5} + 3\xi^{3}\right) + \left(k_{2(1)} + 5k_{1(1)}\right)\xi}{6\left(\xi^{2}-1\right)^{3}} \end{cases}$$

Substituting Eq. (9) into Eq. (8) yields analytical expressions for the thrust and moment of a single-lining tunnel subjected to P waves.

4 Comparison with Numerical Results and Other Analytical Solutions

4.1 Dynamic Time History Analysis Model and Parameters

At present, almost all the existing numerical verification models for the tunnel's analytical solution under seismic are based on quasi-static assumptions [6,26–28]. In reality, the response of a tunnel during an earthquake is inherently dynamic. Therefore, a time-history analysis is performed to verify the proposed analytical solution, taking into account the propagation and scattering of seismic waves. The general finite element software ABAQUS [29] is used for this method.

Fig. 5 shows the 2D finite element model used in this study. The length and width of the ground are 200 m. The tunnel has a circular cross section, and its center is located at the center of the ground. The behavior of the tunnel lining and surrounding ground is assumed to be homogeneous and linearly elastic, as is assumed in the previous analytical solution. Different amounts of lining will be considered in the following subsections, so the corresponding geometry and material properties of the lining will be specified in each section. This study evaluates the applicability of the proposed solution to diverse ground conditions. Three representative ground types are chosen in accordance with Structural Design Code for the Tunnels of Water Intake and Outlet for Nuclear Power Plants (NB/T 20389-2016) [2], which are shown in Table 1.

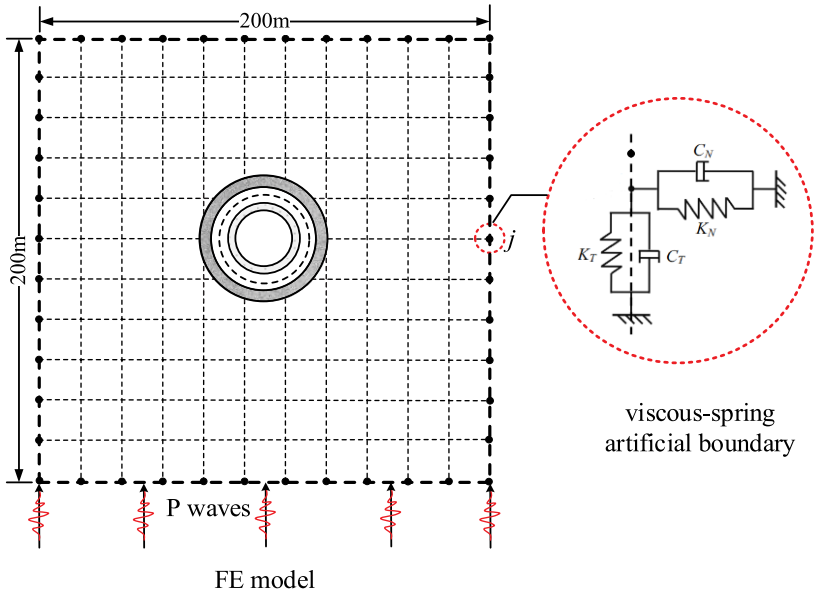

Figure 5: Finite element model with viscous-spring artificial boundary

Table 1: Mechanical parameters of the ground

Grade of surrounding rock	Density ρ_g (kg/m^3)	Young's modulus E_g (GPa)	Poisson's ratio ν_g	Shear wave velocity c_s (m/s)	Compressional wave velocity c_p (m/s)
Case1: soil ($c_p <$ 1000 m/s)	2000	0.054	0.35	100	208

(Continued)

Table 1 (continued)

Grade of surrounding rock	Density ρ_g (kg/m^3)	Young's modulus E_g (GPa)	Poisson's ratio ν_g	Shear wave velocity c_s (m/s)	Compressional wave velocity c_p (m/s)
Case2: soft rock (1000 m/s < $c_p \leq$ 2000 m/s)	2300	1.7	0.3	535	1000
Case3: extremely hard rock (c_p > 4500 m/s)	2500	42	0.25	2598	4600

In the finite element model, both the ground and tunnel are discretized by 8-node isoparametric plane strain solid elements (CPE8R). The dynamic analysis was carried out using an implicit time integration scheme. The time increment was set to 0.01 s, which is consistent with the time step of the input seismic record, ensuring accurate application of the seismic loading and stable numerical integration. In addition, a numerical model convergence analysis was conducted to determine an appropriate mesh size. Although the validation cases presented in this paper adopt the ground material properties of Case 3, the convergence analysis was conservatively performed using Case 1, since lower wave velocities generally require finer meshes to accurately capture seismic wave propagation. The results of the convergence analysis are shown in Fig. 6, where the horizontal axis represents the mesh size, and the vertical axis represents the circumferential stress at the tunnel crown of the lining. It can be observed that when the mesh size is smaller than 4 m, the numerical results become stable, indicating that the numerical model has achieved convergence. Therefore, a mesh size of 2 m was adopted in this study to ensure both numerical accuracy and stability. Furthermore, local mesh refinement was applied in the vicinity of the tunnel to obtain more accurate lining responses while maintaining reasonable computational efficiency for the overall model.

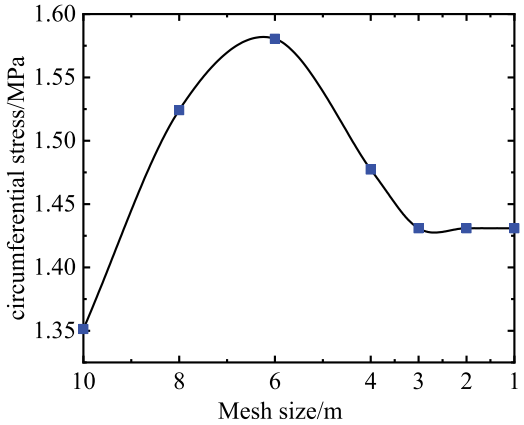

Figure 6: Numerical model convergence analysis with respect to mesh size

The proposed analytical solution has the characteristics of accounting for different interface contact conditions. In order to make the finite element model consistent with the analytical solution,

the terms "Tangential Behavior" and "Normal Behavior" are used to simulate the normal components and tangential components of the interface interaction forces corresponding to various interface contact conditions. For full-slip conditions, the tangential behavior uses a Coulomb friction model with the friction coefficient of 0, and the normal behavior uses a "Hard" contact model which does not allow separation after contact. For no-slip and arbitrary slippage conditions, in addition to maintaining the above setting of no-slip, we introduce a tangential spring connecting two points at the contact interface. The tangential spring stiffness K_s characterizes the interface contact behavior: $K_s \to \infty$ corresponds to a no-slip interface, while $K_s = 0$–∞ corresponds to arbitrary slippage conditions.

It should be noted that, the proposed analytical solution is derived based on the classical assumption that the wavelength corresponding to the dominant earthquake frequency is significantly larger than the tunnel diameter. This allows the seismic load to be idealized as a uniform far-field quasi-static stress. Fundamentally, this implies that the frequency of the seismic wave does influence the accuracy of the analytical solution. This phenomenon is consistent with the observations of Oliaei and Basirat [30] and Hassani et al. [31]. However, Bobet [13], Yu and Wang [18], and Sandoval and Bobet [32] demonstrated that when the wavelength of the dominant earthquake frequency is approximately eight times greater than the tunnel diameter, the error introduced by the quasi-static equivalence method is acceptable. Similarly, results from Huang et al. [16] indicate that when the wavelength-to-diameter ratio exceeds 7, the error of the analytical solution remains below 10%. In engineering practice, the dominant frequency of earthquakes typically ranges from 0.1 to 10 Hz, while the site P wave velocity calculated according to design codes typically ranges from 208 to 4600 m/s. The calculated ratio of wavelength to tunnel diameter ranges from approximately 7 to 1500, which clearly satisfies the long-wavelength assumption. Therefore, under realistic conditions, the actual earthquake frequency has a minor impact on the accuracy of the proposed analytical solution. Consequently, this study utilized a single representative earthquake record solely to verify the consistency between the proposed analytical solution and the reference solution.

In light of the above considerations, a series of numerical models adopts the ground motion record from Takatori Station during the 1995 Hyogoken–Nambu (Kobe) earthquake as the input acceleration history. Although the record is a measured horizontal acceleration component, it is employed in the numerical simulations to generate a vertically propagating plane P wave field through the wave-input procedure and boundary implementation. The corresponding acceleration time history is shown in Fig. 7. The seismic wave input method involves two aspects: (1) the viscous-spring artificial boundary is imposed in the model truncation boundary to absorb the scattered field, as shown in Fig. 5; (2) apply the equivalent node force at the boundary node to realize the free-field input. The specific parameters are calculated as follows.

The viscous-spring artificial boundary consists of a spring and a damper in two directions, which are expressed as follows [33]

$$\begin{cases} K_N = A_j \dfrac{1}{1+A} \dfrac{\lambda + 2G}{l} \\ C_N = A_j B \rho_g c_p \\ K_T = A_j \dfrac{1}{1+A} \dfrac{G}{l} \\ C_T = A_j B \rho_g c_s \end{cases} \tag{10}$$

where subscripts N and T denote the normal and tangential directions of the boundary, respectively. The parameter l is approximately defined as the distance from the geometric center of the structure to the boundary line containing the artificial boundary node j; ρ_g, G, and λ denote the density, shear modulus and Lame constant of the ground, respectively; c_p and c_s denote the primary and shear wave velocities in the ground, respectively; A_j is the area of all elements containing the artificial boundary node j. A and B are correction coefficients, with recommended values of 0.8 and 1.1 [33].

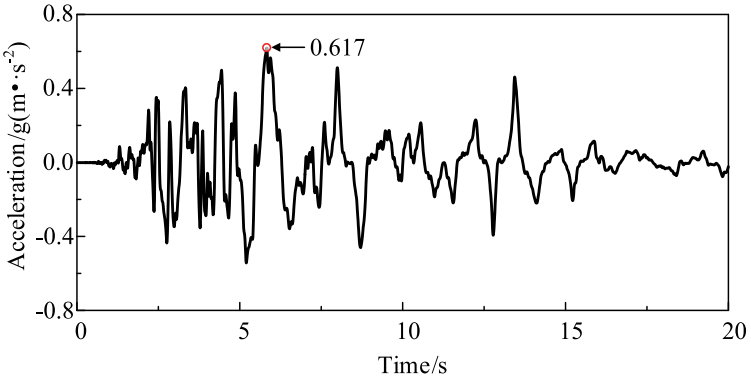

Figure 7: Acceleration time history of the Kobe seismic record of Takatori Station

Following the methodologies proposed by Zhao et al. [34] and Gao et al. [35,36], the seismic loading is converted into equivalent nodal forces acting on the artificial boundary. The earthquake-induced equivalent nodal force $\mathbf{F_B}$ can be expressed as:

$$[\mathbf{F_B}]_j = A_j \boldsymbol{\sigma}_j^f + [\mathbf{K_B}]_j \mathbf{u}_j^f + [\mathbf{C_B}]_j \dot{\mathbf{u}}_j^f \tag{11}$$

where $\mathbf{u}_j^f$, $\dot{\mathbf{u}}_j^f$ and $\boldsymbol{\sigma}_j^f$ are the free-field displacement, velocity and stress on the artificial boundary node j (x_j, y_j), respectively. $\mathbf{K_B}$ and $\mathbf{C_B}$ represent the spring and damping matrices of the viscous-spring boundary, respectively. The computation of $\mathbf{F_B}$ is as follows: (1) The viscous–spring artificial boundary coefficients (K_{Nj}, K_{Tj}, C_{Nj}, C_{Tj}) are calculated using Eq. (10) and assembled into the global boundary stiffness matrix $\mathbf{K_B}$ and boundary damping matrix $\mathbf{C_B}$. (2) The layered soil profile and the corresponding material parameters, together with the incident P wave record, are specified. Then, using a one-dimensional free-field analysis program, the free-field displacement $\mathbf{u}_j^f$, free-field velocity $\dot{\mathbf{u}}_j^f$, and free-field stress $\boldsymbol{\sigma}_j^f$ at the location associated with boundary node j are obtained. (3) After completing the above steps, the equivalent boundary nodal force $\mathbf{F_B}$ is computed according to Eq. (11) and applied as external nodal loads at the corresponding artificial boundary node locations in the finite element model.

It should be emphasized that the proposed solution and the finite element model differ fundamentally in nature and purpose. The proposed model is a closed-form analytical formulation derived from elasticity theory, in which the P wave incidence is equivalently represented by far-field stresses and further decomposed into hydrostatic and pure shear components. Each lining layer is modeled as a thick-walled cylinder, and an interfacial tangential spring stiffness K_i is introduced at the ground-lining and lining-lining interfaces to account for full-slip, no-slip, and arbitrary contact conditions. In contrast, the finite element model is a numerical dynamic time-history simulation (ABAQUS) that discretizes the ground-tunnel system and directly computes transient wave propagation and scattering under a seismic input record, with a viscous-spring artificial boundary to truncate the domain. Therefore, the time-history finite element model simulation is adopted as the reference solution to

quantify the true prediction error of the proposed pseudo-static analytical model and to validate its accuracy under realistic seismic loading.

4.2 Verification for Case of Tunnel with Single Lining

In this section, a water intake tunnel with a single lining is selected for verification. The proposed analytical solution is compared with Bobet's solution and numerical analysis results to verify the accuracy and validity. The benchmark reference is established through the dynamic time-history analysis detailed in Section 4.1. The mechanical properties of the tunnel lining are considered constant, with a density of 2500 kg/m^3, a Young's modulus of 4.5 GPa, and a Poisson's ratio of 0.25. The seismic record of the Kobe earthquake, presented in Fig. 6, is applied to the bottom boundary of the numerical model as vertically propagating P waves.

4.2.1 Cases of Different Lining Thicknesses

In this study, the tunnel lining is modeled as a thick-walled cylindrical structure. To evaluate the validity of the analytical solution for various lining thicknesses, the lining thickness t is assigned values of 0.3, 0.6, and 0.9 m, while the outer radius of the lining is maintained at 3 m. The mechanical parameters of the ground are set to Case3 in Table 1. In addition, the tangential stiffness coefficient K_i at the ground-tunnel contact interface is set to 0, 1e^8 and 1e^{16}, corresponding to full-slip, middle slip (mid-slip) and no-slip contact conditions, respectively. It should be noted that in the following, T_{max} and M_{max} are defined as the absolute maximum values of the lining thrust and moment, respectively, obtained over the entire duration of the earthquake motion.

Fig. 8 illustrates the variations of the peak thrust T_{max} and peak moment M_{max} along the tunnel cross-section, obtained from the proposed analytical solution, the widely adopted Bobet's method, and numerical simulations under vertically incident P waves. The analysis considers different lining thicknesses and interface contact conditions. It should be noted that, as Bobet's method only accounts for the no-slip and full-slip interfaces, the corresponding results for the mid-slip case are not available.

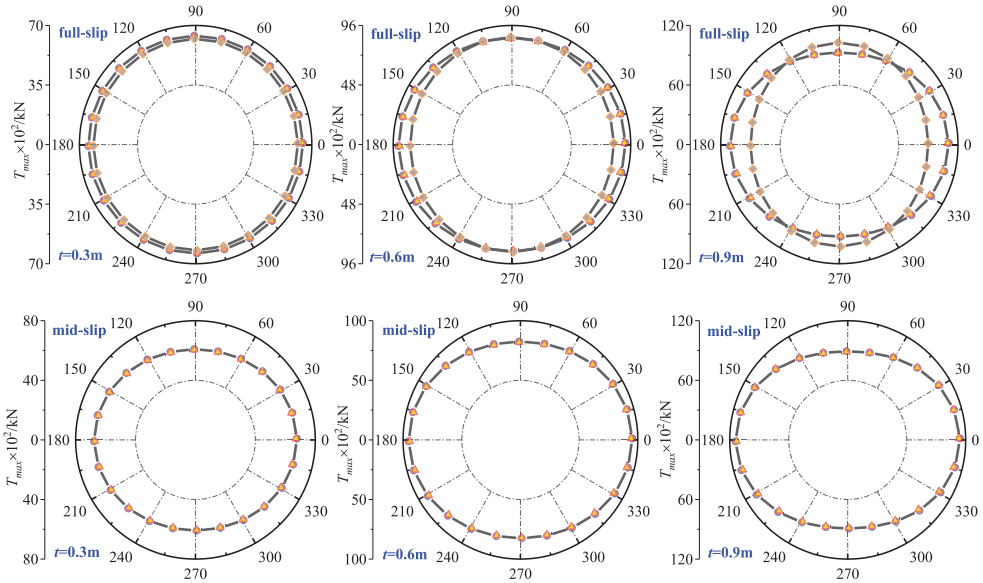

Figure 8: (Continued)

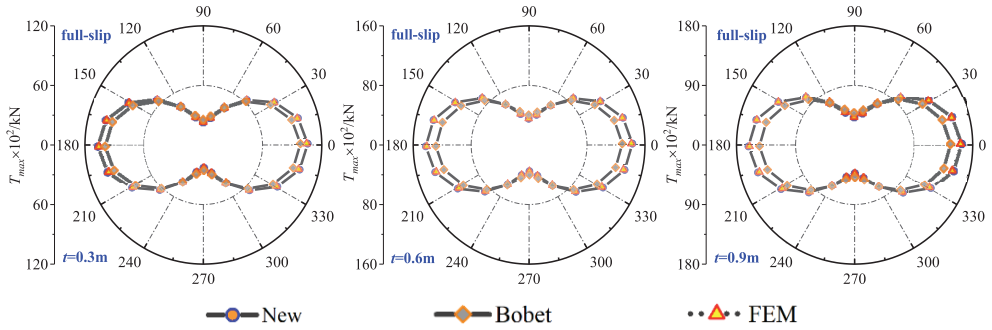

(a)

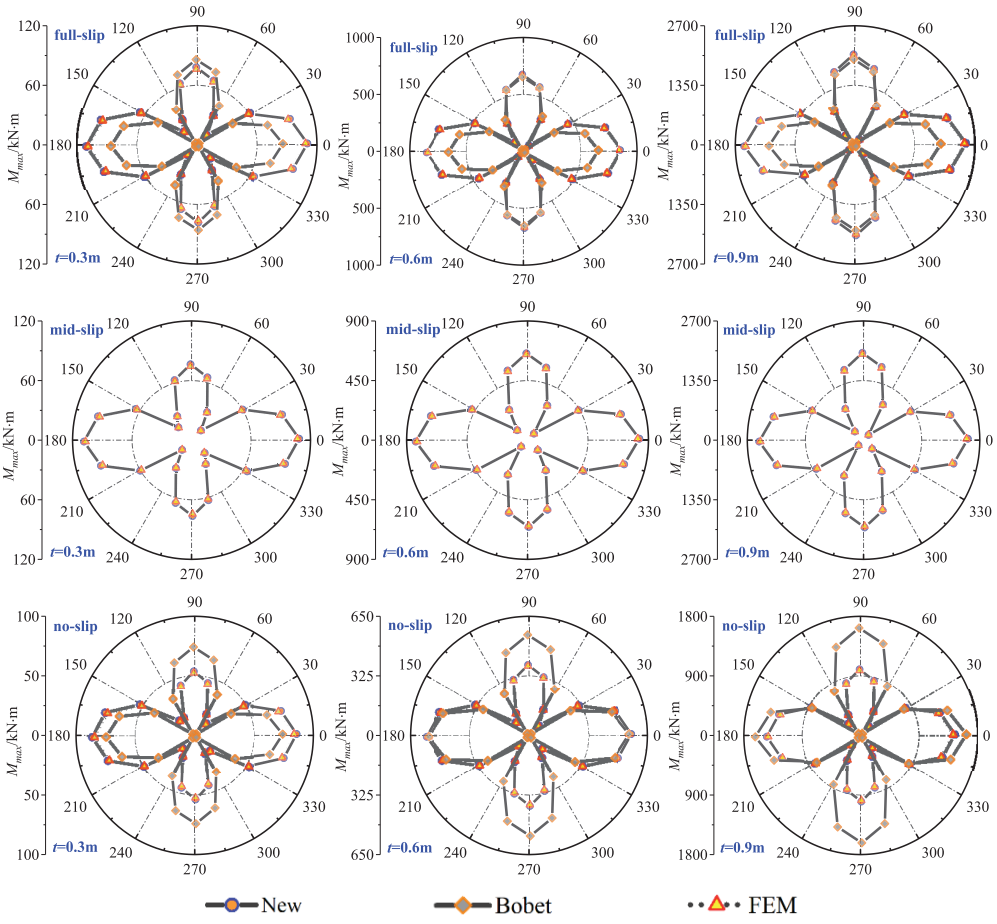

(b)

Figure 8: Distribution of peak thrust and moment of lining under P waves with considering different lining thicknesses and interface contact conditions: (a) Peak thrust T_{max}; (b) Peak moment M_{max}

Fig. 8 shows that the thrust and moment of the proposed analytical solution, Bobet's solution and the numerical analysis have the same distribution. The numerical analysis results and analytical solution show that the maximum values of the thrust and moment are located at the haunch. Moreover, when the contact condition changes, the thrust distribution of the tunnel will change, but the moment

distribution is almost invariant. This is because the moment corresponds to the deformation shape of the tunnel, and the contact condition has little influence on the deformation shape. Regardless of the thickness of the lining or the contact conditions, there is an excellent agreement between the proposed analytical solution and the numerical analysis results. However, the errors of the Bobet's solution are significant, especially in the case of thick lining. Compared with the classical analytical solution, the proposed analytical solution has obvious advantages in the case of thick lining and can take into account different contact conditions.

4.2.2 Cases of Different Ground Conditions

Previous studies have shown that ground conditions greatly influence the seismic response of the structure [37–39]. Three ground conditions are selected to verify the applicability of the proposed analytical solution under different ground conditions, and the mechanical parameters are shown in Table 1. The outer radius of the tunnel is 3 m, the lining thickness is 0.3 m. As in Section 4.2.1, the contact conditions of the ground-lining interface are set as full-slip, mid-slip, and no-slip.

Fig. 9 illustrates the variations of the peak thrust T_{max} and peak moment M_{max} along the tunnel cross-section, obtained from the proposed analytical solution, the widely adopted Bobet's method, and numerical simulations under vertically incident P waves. The analysis considers different ground conditions and interface contact conditions. It can be clearly observed that the thrust and moment obtained from the proposed analytical solution perfect match with the numerical results, with differences do not exceeding 2% for all cases. When the ground is soft to hard, the proposed analytical solution still keeps high precision, which shows that proposed analytical solutions have good applicability under different ground conditions. It should be noted that the difference between Bobet's solution and the numerical analysis results is significant. It can be seen from the above comparison that the proposed analytical solution has more advantages than the classical analytical solution. As shown in Fig. 9, a similar trend to that in Section 4.2.1 is observed, where the moment distribution of the tunnel is nearly unaffected by variations in the contact conditions.

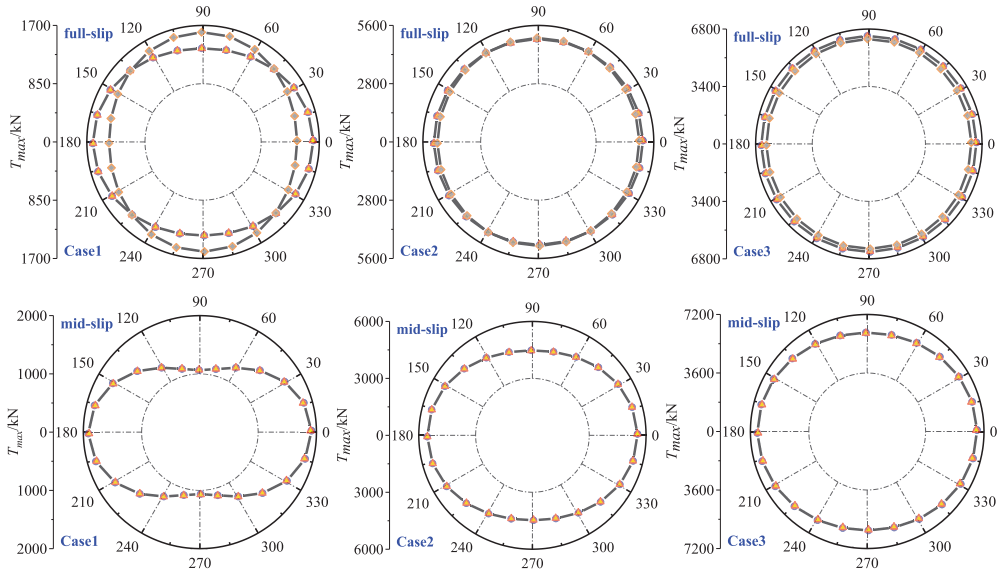

Figure 9: (Continued)

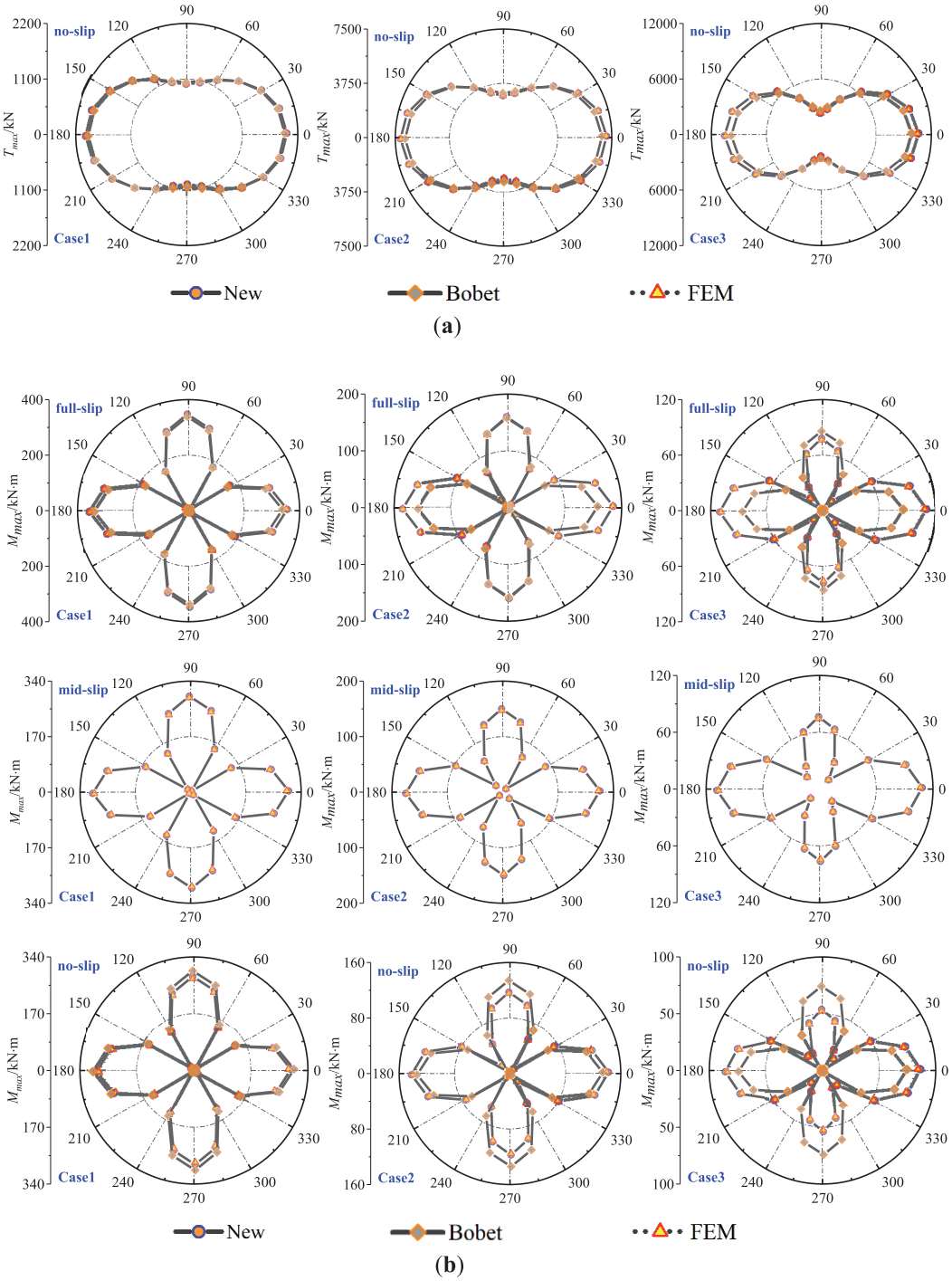

Figure 9: Distribution of peak thrust and moment of lining under P waves with considering different ground conditions and interface contact conditions: (a) Peak thrust T_{max}; (b) Peak moment M_{max}

4.3 Verification for Case of Tunnel with Double Linings

This section further verifies the accuracy of the proposed analytical solution. The dynamic time history analysis method described in Section 4.1 is used as the reference solution. A water intake tunnel with a double-layer lining is chosen as the subject of this investigation. The tunnel features a circular cross-section, consisting of a primary and a secondary lining. The inner radius is 4.15 m, with thicknesses of 0.25 and 0.6 m for the primary and secondary linings, respectively. The mechanical properties of the linings and surrounding ground are summarized in Table 2. The interfaces between the ground and the primary lining, and between the primary and secondary linings are idealized as a no-slip contact condition.

Table 2: Mechanical parameters of surrounding ground and linings

Object	Young's modulus	Poisson's ratio	Density
Primary lining	28 GPa	0.2	2500 kg/m^3
Secondary lining	30 GPa	0.2	2500 kg/m^3
Surrounding ground	7.5 GPa	0.28	2930 kg/m^3

Fig. 10 presents a comparison between the analytical solution and the numerical analysis results for the peak thrust and moment of the lining under P waves. Again, the agreement between the proposed analytical solution and the numerical results is good. Moreover, the distribution of thrust and moment of primary lining and secondary lining is consistent, and the maximum value is located at the haunch. The comparison results clearly demonstrate that the proposed analytical solutions yield accurate and dependable predictions of the thrust and moment in the composite tunnel.

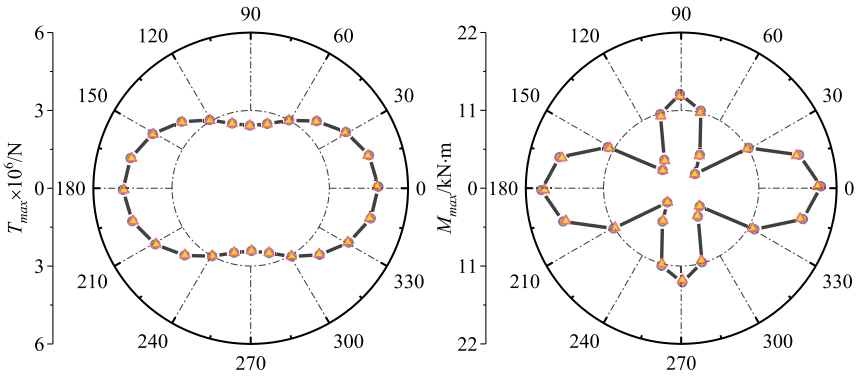

(a)

Figure 10: (Continued)

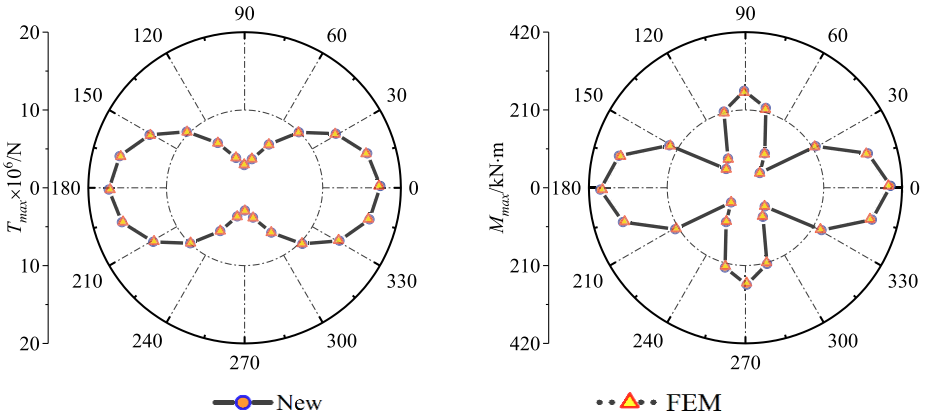

(b)

Figure 10: Distribution of peak thrust T_{max} and peak moment M_{max} of composite tunnel under P waves: (a) Primary lining; (b) Secondary lining

5 Parameters Analysis

5.1 Effect of Tangential Stiffness Coefficient K_i

The analytical solution proposed in this study introduces the tangential stiffness coefficient K_i to account for the slippage effects at all interfaces within the ground-lining system. Accordingly, this section investigates the influence of K_i on the lining thrust and moment. For the convenience of analysis, the study object is a single lining tunnel with only one contact interface. The geometric and mechanical properties of the ground and lining remain consistent with those described in Section 4.2.2.

Fig. 11 presents the normalized thrust and moment of the lining under P waves for different tangential stiffness coefficients K_i and three ground conditions. As shown in Fig. 11, with the increase of the tangential stiffness coefficient K_i, the normalized thrust increases and the normalized moment decreases, regardless of the ground conditions. The figure shows that, regardless of the ground condition, the normalized thrust increases while the normalized bending moment decreases with increasing tangential stiffness coefficient K_i (corresponding to a transition of the contact state from full-slip to no-slip). In theory, the tangential stiffness coefficient K_i, varying from 0 to ∞, influences the tunnel's seismic internal forces. However, the figure shows that its effective influence is confined to a relatively narrow range (10^3–10^{12}). In addition, as the ground stiffness increases from soft to hard, the effective influence range of K_i progressively broadens. Based on these findings, practical recommendations for selecting K_i in engineering design can be provided. Specifically, when the interface contact condition is unknown, it is recommended to adopt $K_i = 10^3$ and $K_i = 10^{12}$ to perform an envelope analysis, thereby capturing the upper and lower bounds of thrust and moment. When the interface condition can be determined from field measurements or project-specific data, the use of the measured K_i value is recommended to obtain more accurate and realistic design results.

The above findings provide valuable guidance for engineering design. In water intake tunnels, a smooth waterproof layer is commonly installed between the lining and the surrounding rock to reduce water leakage. However, this configuration decreases the interface contact stiffness, which consequently increases the moment within the lining. Under such conditions, it is advisable to appropriately increase the reinforcement ratio or fiber content to enhance the flexural strength of the lining, thereby ensuring structural safety.

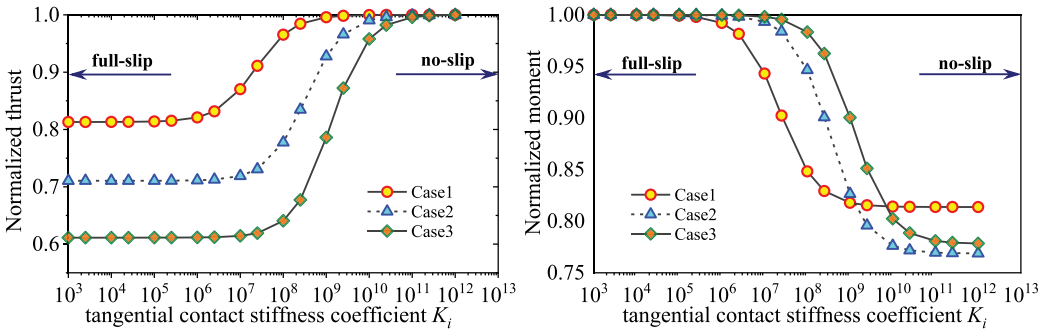

Figure 11: Effect of K_i on normalized thrust and moment distribution under different ground conditions

5.2 Effect of Flexibility Ratio between Ground and Tunnel

Many previous studies have shown that the relative stiffness between the ground and the tunnel has a great influence on the response of the tunnel [6,12,13,27]. The flexibility ratio F proposed by Wang [7] is used to characterize the relative stiffness between the tunnel and the surrounding ground:

$$F = \frac{E_g\left(1-\nu_l^2\right)r^3}{6E_lI\left(1+\nu_g\right)} \tag{12}$$

where E_g, ν_g, and E_l, ν_l, are the Young's modulus and Poisson's of the ground and tunnel, respectively. I and r are the moment of inertia and the outer radius of the tunnel, respectively.

In this section, the effect of the flexibility ratio F on the thrust and moment of the tunnel is studied by using the proposed analytical solution. For convenience, the research object is a tunnel with a single lining. The geometric and mechanical parameters of the tunnel are the same as in Section 4.2.2, and the soil deformation induced by the P waves is kept constant. The ground is considered as a linear elasticity with Poisson's ratio $\nu_g = 0.2$ and density $\rho_g = 2500$ kg/m^3, while its Young's modulus is variable, resulting in a flexibility ratio F in the range of 0.1 to 1000 (Table 3). In addition, three types of contact conditions are considered at the ground-lining interface, including no-slip, mid-slip, and full-slip cases.

Table 3: Mechanical properties of the ground and corresponding flexibility ratio

Young's modulus E_g (MPa)	Flexibility ratio F
1.953	0.1
7.813	0.4
19.531	1
48.828	2.5
117.188	6
195.313	10
585.937	30
1367.188	70
1953.125	100

(Continued)

Table 3 (continued)

Young's modulus E_g (MPa)	Flexibility ratio F
3906.250	200
9765.625	500
19,531.25	1000

The results presented in Fig. 12 indicate that the flexibility ratio has a significant influence on the seismic response of the tunnel. As the flexibility ratio F increases, both the maximum thrust and moment decrease, exhibiting a typical nonlinear relationship. From a mechanical perspective, when F is small (i.e., the tunnel structure is relatively stiff), the deformation compatibility between the tunnel and the surrounding ground is poor. Under seismic excitation, most deformation of the ground is transmitted to the tunnel, resulting in large internal forces. As F increases, the deformation of the tunnel and surrounding ground becomes more compatible, allowing the soil to absorb part of the earthquake-induced deformation. This improved compatibility reduces the demand on the structure, thereby decreasing the internal forces. Moreover, changes in the contact condition do not affect the overall variation trend of axial force and bending moment with the flexibility ratio but only influence their magnitudes.

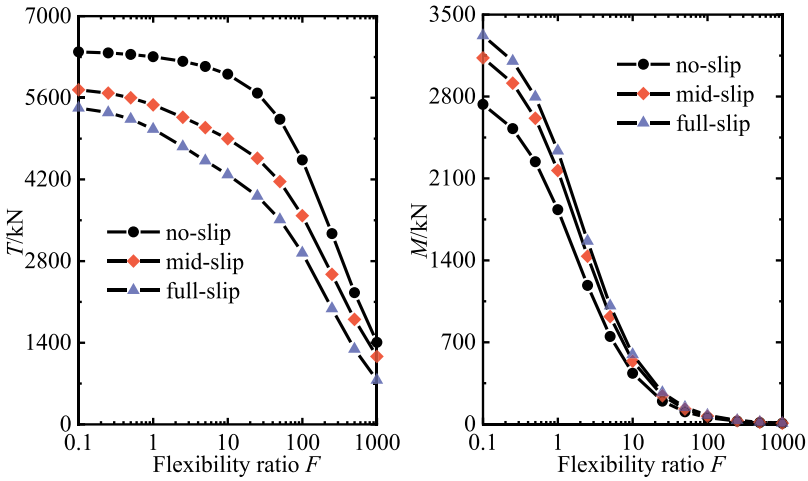

Figure 12: Effect of F on thrust and moment of tunnel with considering different contact conditions

From an engineering design viewpoint, the flexibility ratio should be carefully controlled according to the ground stiffness and structural type. For rigid linings, increasing the flexibility (e.g., by introducing a damping layer or a compressible interface) can help mitigate excessive internal forces under seismic loading. For flexible systems, such as segmental linings or structures with compressible joints, it is important to prevent overly high flexibility that could lead to excessive deformation.

5.3 Effect of Isolation Layer

To reduce the damage to the tunnel caused by the earthquake, an isolation layer is often placed between the surrounding ground and the concrete lining. Previous studies [5] have demonstrated that

both the material type and thickness of the isolation layer significantly affect the dynamic response of tunnels. Therefore, this section uses the proposed analytical solution to explore the effect of different isolation layer materials and thicknesses on the thrust and moment of the tunnel. The isolation layer is considered a thick-walled cylinder, its shear modulus and the ratio of surrounding ground modulus are G_i/G_g, ranging from 0.001 to 1. The ratio of isolation layer thickness t_i to tunnel outer radius r_1 ranges from 0.05 to 0.2, covering most of the cases in the literature. The tunnel's dimensions and mechanical properties, and the mechanical properties of the ground, are the same as those used in Section 4.2.2. According to the parameter analysis of Section 5.1, the tunnel response is between full-slip and no-slip. Therefore, the contact condition between the tunnel and isolation layer in this section is set as full-slip and no-slip.

Figs. 13 and 14 provide the effects of modulus ratio G_i/G_g on maximum thrust and moment of tunnel with different thickness ratios t_i/r_1 for no-slip and full-slip contact conditions. The results indicate that the isolation layer has a significant influence on the thrust and moment of the lining. The isolation layer can effectively reduce the thrust of the tunnel, and with the G_i/G_g from 1 to 0.001, namely, as the isolation layer becomes progressively softer, the thrust of the tunnel gradually decreases. It can be noted that the thicker isolation layer has a better effect on reducing the thrust of the tunnel. In different ground conditions and different contact conditions, the change of thrust is the same, but the moment is different. More specifically, as the isolation layer gradually becomes soft, the moment of the tunnel tends to increase first and then decrease. That is to say, there is a most unfavorable modulus ratio, which leads to the maximum bending moment of the tunnel. For the no-slip case, the value of the most unfavorable modulus ratio decreases with the decrease of the thickness of the isolation layer, while for the full-slip case, the most unfavorable modulus ratio does not seem to change with the thickness of the isolation layer. In addition, for reducing the moment value, it is not that the thicker the isolation layer is, the better the effect will be. When the modulus ratio is greater than a certain critical value, the thicker isolation layer will increase the moment, and the critical value will decrease with the hardening of the ground.

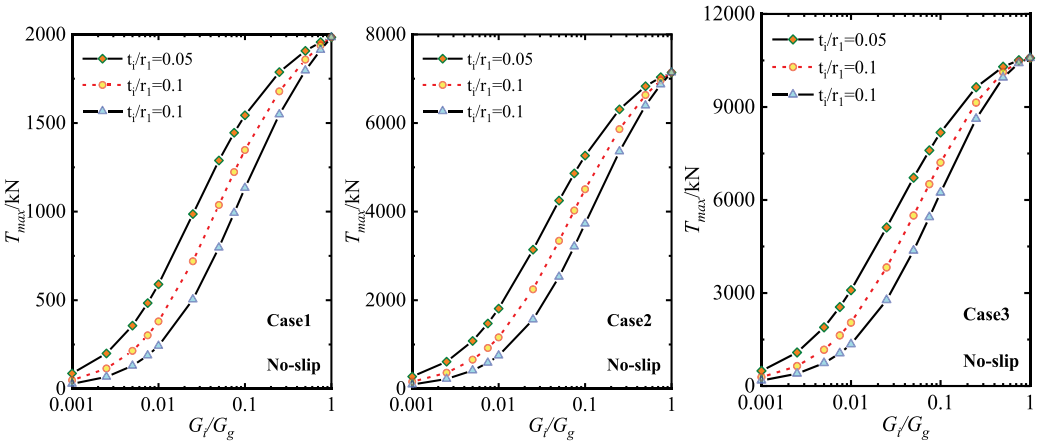

Figure 13: (Continued)

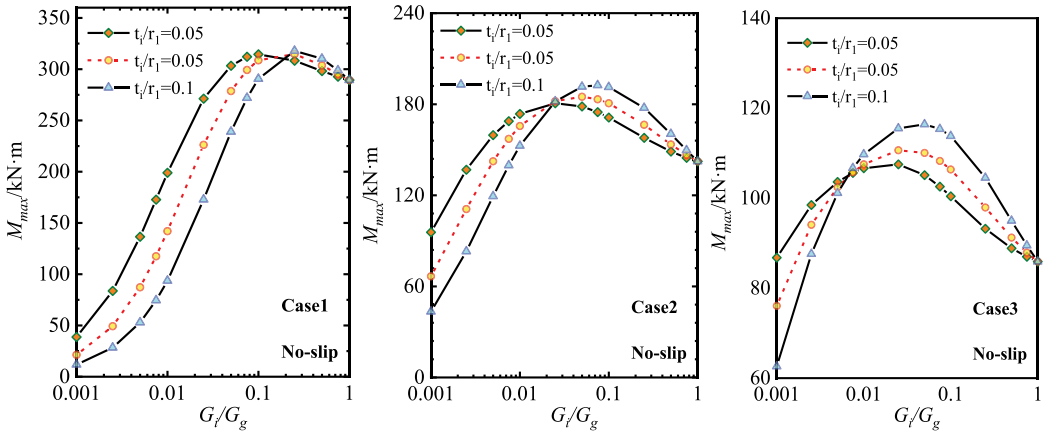

Figure 13: Effect of modulus ratio G_t/G_g on maximum thrust and moment of tunnel with different thickness ratios t_i/r_1 for no-slip condition

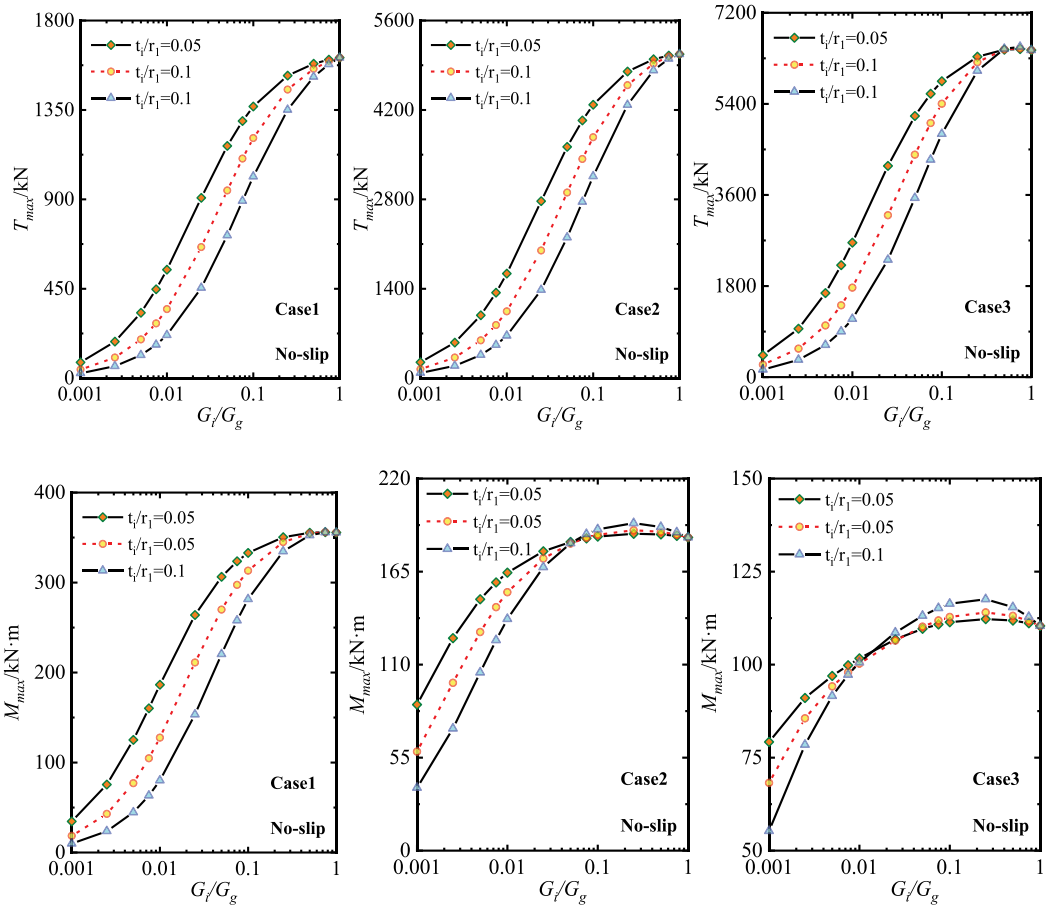

Figure 14: Effect of modulus ratio G_t/G_g on maximum thrust and moment of tunnel with different thickness ratios t_i/r_1 for full-slip condition

6 Conclusions

This study develops an analytical solution for internal forces of intake and outlet tunnels in nuclear power plants with an arbitrary number of lining layers subjected to far-field stresses induced by P waves. The main novel contributions of this work are threefold. (1) The solution is applicable to tunnels with an arbitrary number of lining layers, which is particularly relevant for practical nuclear power plant tunnels that frequently adopt double linings or composite lining systems. (2) Each lining layer is modeled as a thick-walled cylinder, enabling reliable prediction for thick linings where conventional beam or shell-based analytical solutions can induce non-negligible errors. (3) A spring-type tangential stiffness coefficient K_i is introduced at both the ground–lining and lining–lining interfaces, allowing the model to represent not only the idealized full-slip and no-slip conditions but also intermediate contact states. These features collectively extend existing P wave analytical solutions and improve their engineering realism for nuclear power plant tunnel systems. The accuracy and applicability of the proposed analytical solution are validated through comparisons with numerical analysis results and Bobet's solution. The comparison reveals that the proposed approach has excellent performance and outperforms traditional analytical solutions, making it can be used in the preliminary seismic design of nuclear power plant intake and outlet tunnels.

In addition, the effect of tangential stiffness coefficient K_i, flexibility ratio F, and isolation layer on the seismic response of the water intake tunnel is also discussed by the proposed analytical solution, the following conclusions can be drawn:

(1) An increase in the tangential stiffness coefficient K_i at the ground-lining interface results in greater tunnel thrust, while simultaneously leading to a decrease in the tunnel moment. The effective influence range of the tangential stiffness coefficient K_i on the tunnel's internal force is limited to a narrow area, and this range progressively broadens as the ground stiffness increases from soft to hard. These findings suggest that the interfacial stiffness plays a crucial role in determining tunnel performance. When the actual interface condition is uncertain, an envelope analysis using representative lower/upper bounds of K_i can be adopted to bound internal-force demands, which is useful for conservative nuclear power plant safety-related design. In practical engineering applications, waterproofing and smooth interlayers may increase bending demand. In nuclear power plant intake or outlet tunnels, waterproof layers or smooth interfaces are commonly used for seepage control; however, such treatments reduce tangential interfacial stiffness and may amplify moment demand. Therefore, for tunnels with waterproof layers or low interface roughness, it is advisable to enhance flexural capacity through reinforcement optimization and/or material toughening measures (e.g., fiber reinforcement), rather than relying solely on thrust-controlled design.

(2) The compliance ratio F represents the relative stiffness between the ground and the tunnel, which has a controlling effect on the internal forces of the tunnel. As F increases, both the maximum thrust and moment decrease due to improved deformation compatibility between the tunnel and the surrounding ground. When F is small, the tunnel behaves rigidly, and poor compatibility leads to higher internal stresses under seismic excitation. Conversely, higher F values promote coordinated deformation and lower internal lining forces. From an engineering standpoint, improving deformation compatibility—through lining stiffness adjustment or rational interface design—can effectively reduce seismic internal-force demand. However, excessively flexible systems should be avoided where serviceability or deformation control is critical.

(3) There is a significant mitigation effect on the tunnel's thrust induced by P waves for a softer and thicker isolation layer. However, the trend for the moment is different. As the isolation layer

becomes softer and the moment increases first and then decreases, there exists a most unfavourable modulus ratio G_l/G_g between the isolation layer and the ground. Moreover, there is a critical modulus ratio, when the modulus ratio is greater than the critical value, the thicker isolation layer will increase the moment. Hence, the isolation layer should be carefully designed to balance thrust reduction and moment control, avoiding over-softening or excessive thickness.

Acknowledgement: The authors express their gratitude to Young Talents Research Project of China National Nuclear Corporation and Scientific Research Fund Project of China Nuclear Power Engineering Co., Ltd.

Funding Statement: This research was funded by the Young Talents Research Project of China National Nuclear Corporation (KY25116) and Scientific Research Fund Project of China Nuclear Power Engineering Co., Ltd. (KY25107).

Author Contributions: The authors confirm contribution to the paper as follows: Conceptualization, Yawei Duan, Lihua Wu, Dongyang Wang, Rongpeng Li and Di Jiang; methodology, Yawei Duan, Lihua Wu; validation, Yawei Duan, Lihua Wu, Dongyang Wang; investigation, Yawei Duan; writing—original draft preparation, Yawei Duan; writing—review and editing, Rongpeng Li and Di Jiang; visualization, Yawei Duan; supervision, Di Jiang; funding acquisition, Yawei Duan, Dongyang Wang. All authors reviewed and approved the final version of the manuscript.

Availability of Data and Materials: The data that support the findings of this study are available from the Corresponding Author, [Di Jiang], upon reasonable request.

Ethics Approval: Not applicable.

Conflicts of Interest: The authors declare no conflicts of interest.

References

1. GB. Standard for seismic design of nuclear power plants. Beijing, China: Ministry of Housing and Urban-Rural Development of the People's Republic of China; 2019. (In Chinese).
2. NB/T. Institute of nuclear industry standardization. structural design code for the tunnels of water intake and outlet for nuclear power plants. Beijing, China: National Energy Administration; 2016. (In Chinese).
3. Huo H, Bobet A, Fernández G, Ramírez J. Load transfer mechanisms between underground structure and surrounding ground: evaluation of the failure of the Daikai Station. J Geotech Geoenviron Eng. 2005;131(12):1522–33.
4. Wang WL, Wang TT, Su JJ, Lin CH, Seng CR, Huang TH. Assessment of damage in mountain tunnels due to the Taiwan Chi-Chi Earthquake. Tunn Undergr Space Technol. 2001;16(3):133–50. doi:10.1016/S0886-7798(01)00047-5.
5. Li T. Damage to mountain tunnels related to the Wenchuan earthquake and some suggestions for aseismic tunnel construction. Bull Eng Geol Environ. 2012;71(2):297–308. doi:10.1007/s10064-011-0367-6.
6. Kontoe S, Avgerinos V, Potts DM. Numerical validation of analytical solutions and their use for equivalent-linear seismic analysis of circular tunnels. Soil Dyn Earthq Eng. 2014;66(4):206–19. doi:10.1016/j.soildyn.2014.07.004.
7. Wang JN. Seismic design of tunnels. New York, NY, USA: Parsons Brinckerhoff Quade & Douglas, Inc.; 1993.

8. Penzien J, Wu CL. Stresses in linings of bored tunnels. Earthq Eng Struct Dyn. 1998;27(3):283–300. doi:10.1002/(SICI)1096-9845(199803)27:3<283::AID-EQE732>3.0.CO;2-T.
9. Penzien J. Seismically induced racking of tunnel linings. Earthq Eng Struct Dyn. 2000;29(5):683–91. doi:10.1002/(SICI)1096-9845(200005)29:5<683::AID-EQE932>3.0.CO;2-1.
10. Hashash YMA, Hook JJ, Schmidt B, I-Chiang Yao J. Seismic design and analysis of underground structures. Tunn Undergr Space Technol. 2001;16(4):247–93. doi:10.1016/S0886-7798(01)00051-7.
11. Basirat R, Salari-rad H, Molladavoodi H. Analysis of the monolithic and segmental tunnel lining under earthquake loading. Ingegneria Sismica. 2019;36(4):140–55.
12. Park KH, Tantayopin K, Tontavanich B, Owatsiriwong A. Analytical solution for seismic-induced ovaling of circular tunnel lining under no-slip interface conditions: a revisit. Tunn Undergr Space Technol. 2009;24(2):231–5. doi:10.1016/j.tust.2008.07.001.
13. Bobet A. Effect of pore water pressure on tunnel support during static and seismic loading. Tunn Undergr Space Technol. 2003;18(4):377–93. doi:10.1016/S0886-7798(03)00008-7.
14. Jayasinghe JASC, Hori M, Riaz MR, Wijerathne MLL, Ichimura T. Conversion between solid and beam element solutions of finite element method based on meta-modeling theory: development and application to a ramp tunnel structure. Earthq Eng Eng Vib. 2017;16(2):297–309. doi:10.1007/s11803-017-0383-z.
15. Lin Y. A shield tunnel model based on generalized-node solid-shell and spacial joint element. In: Proceedings of GeoShanghai 2018 International Conference: Tunnelling and Underground Construction. Singapore: Springer; 2018. p. 460–7. doi:10.1007/978-981-13-0017-2_46.
16. Huang J, Shao W, Zhao M, Han J, Zhao X, Du X, et al. Simplified analytical solution for circular tunnel under obliquely incident SV wave. Soil Dyn Earthq Eng. 2021;140(3):106429. doi:10.1016/j.soildyn.2020.106429.
17. El Naggar H, Hinchberger SD, El Naggar MH. Simplified analysis of seismic in-plane stresses in composite and jointed tunnel linings. Soil Dyn Earthq Eng. 2008;28(12):1063–77. doi:10.1016/j.soildyn.2007.12.001.
18. Yu H, Wang Q. Analytical solution for deep circular tunnels covered by an isolation coating layer subjected to far-field shear stresses. Tunn Undergr Space Technol. 2021;115:104026. doi:10.1016/j.tust.2021.104026.
19. Lin CH, Lee VW, Todorovska MI, Trifunac MD. Zero-stress, cylindrical wave functions around a circular underground tunnel in a flat, elastic half-space: incident P-waves. Soil Dyn Earthq Eng. 2010;30(10):879–94. doi:10.1016/j.soildyn.2010.01.010.
20. Zou Y, Liu H, Jing L, Miao Y. Response of circular tunnel with imperfect interface bonding in layered ground subjected to obliquely incident plane P or SV wave. Int J Numer Anal Meth Geomech. 2018;42(16):2001–17. doi:10.1002/nag.2844.
21. Huang J, Zhao M, Du X. Non-linear seismic responses of tunnels within normal fault ground under obliquely incident P waves. Tunn Undergr Space Technol. 2017;61(2):26–39. doi:10.1016/j.tust.2016.09.006.
22. Qiu D, Chen J, Xu Q. Dynamic responses and damage forms analysis of underground large scale frame structures under oblique SV seismic waves. Soil Dyn Earthq Eng. 2019;117(4):216–20. doi:10.1016/j.soildyn.2018.11.032.
23. Basirat R. Analysis of tunnel lining internal forces under the influence of S and P-waves: an analytical solution and quasi-static numerical method. Rock Mech Bull. 2025;4(1):100168. doi:10.1016/j.rockmb.2024.100168.
24. Kouretzis GP, Sloan SW, Carter JP. Effect of interface friction on tunnel liner internal forces due to seismic S- and P-wave propagation. Soil Dyn Earthq Eng. 2013;46(11):41–51. doi:10.1016/j.soildyn.2012.12.010.
25. Butscher C. Steady-state groundwater inflow into a circular tunnel. Tunn Undergr Space Technol. 2012;32(2–4):158–67. doi:10.1016/j.tust.2012.06.007.
26. Hashash YMA, Park D, Yao JIC. Ovaling deformations of circular tunnels under seismic loading, an update on seismic design and analysis of underground structures. Tunn Undergr Space Technol. 2005;20(5):435–41. doi:10.1016/j.tust.2005.02.004.

27. Lu S, Xu H, Wang L, Liu S, Zhao D, Nie W. Effect of flexibility ratio on seismic response of rectangular tunnels in sand: experimental and numerical investigation. Soil Dyn Earthq Eng. 2022;157(4):107256. doi:10.1016/j.soildyn.2022.107256.
28. Bin J. Study on the simplified analysis methods of seismic effects of underground structures. Recent Dev World Seismol. 2017;5:42–3. (In Chinese).
29. Karlson H, Sorensen. ABAQUS, finite element program. Pawtucket, RI, USA: Hibbit, Karlson & Sorensen Inc.; 2009.
30. Oliaei M, Basirat R. The effect of earthquake frequency content on the internal forces in the tunnels permanent lining. J Earthq Eng. 2022;26(2):817–36. doi:10.1080/13632469.2019.1693445.
31. Hassani R, Hojatkashani A, Basirat R. Nonlinear seismic analysis of ground structure to evaluate the capacity of a permanent tunnel lining. Struct Eng Int. 2024;34(1):102–13. doi:10.1080/10168664.2022.2125485.
32. Sandoval E, Bobet A. Effect of input frequency on the seismic response of deep circular tunnels. Soil Dyn Earthq Eng. 2020;139:106421. doi:10.1016/j.soildyn.2020.106421.
33. Du XL, Zhao M, Wang JT. A stress artificial boundary in fea for near-field wave problem. Chin J Theor Appl Mech. 2006;38(1):49–56. (In Chinese).
34. Zhao M, Yin H, Du X, Liu J, Liang L. 1D finite element artificial boundary method for layered half space site response from obliquely incident earthquake. Earthq Struct. 2015;9(1):173–94. doi:10.12989/eas.2015.9.1.173.
35. Gao Z, Zhao M, Huang J, Du X, Wu L. Three-dimensional nonlinear seismic response analysis of subway station crossing longitudinally inhomogeneous geology under obliquely incident P waves. Eng Geol. 2021;293(6):106341. doi:10.1016/j.enggeo.2021.106341.
36. Gao Z, Zhao M, Du X, Zhong Z. A generalized response spectrum method for seismic response analysis of underground structure combined with viscous-spring artificial boundary. Soil Dyn Earthq Eng. 2021;140(3):106451. doi:10.1016/j.soildyn.2020.106451.
37. Duan Y, Huang J, Zhao M, Zhao X, Li H, Du X. Numerical validation of analytical solutions for tunnels and their applicability evaluation index. Soil Dyn Earthq Eng. 2023;174(4):108206. doi:10.1016/j.soildyn.2023.108206.
38. Li H, Zhao M, Huang J, Liao W, Ma C, Zhao X. Analytical solution for circular tunnel under obliquely incident shear waves. Soil Dyn Earthq Eng. 2023;171(1):107946. doi:10.1016/j.soildyn.2023.107946.
39. Sun Z, Zhang D, Li A, Lu S, Tai Q, Chu Z. Model test and numerical analysis for the face failure mechanism of large cross-section tunnels under different ground conditions. Tunn Undergr Space Technol. 2022;130(1):104735. doi:10.1016/j.tust.2022.104735.

Appendix A

Under axisymmetric loading, the stress function for the models presented in Fig. 3b,c is a function of the radial coordinate ρ only, namely,

$$\Phi = \Phi(\rho) \tag{A1}$$

The compatibility relation in polar coordinates is given by

$$\left(\frac{\partial^2}{\partial\rho^2} + \frac{1}{\rho}\frac{\partial}{\partial\rho} + \frac{1}{\rho^2}\frac{\partial^2}{\partial\varphi^2}\right)^2 \Phi = 0 \tag{A2}$$

Substituting the stress function into the compatibility relation and integrating yields the general solution of the stress function as

$$\Phi(\rho) = A\ln\rho + B\rho^2\ln\rho + C\rho^2 + D \tag{A3}$$

where, A, B, C, D denote constants to be determined from boundary and continuity conditions.

The corresponding stress components expressed by the stress function in polar coordinates as follows

$$\sigma_\rho = \frac{A}{\rho^2} + B\left(1 + 2\ln\rho\right) + 2C \tag{A4a}$$

$$\sigma_\varphi = -\frac{A}{\rho^2} + B\left(3 + 2\ln\rho\right) + 2C \tag{A4b}$$

$$\tau_{\rho\varphi} = \tau_{\varphi\rho} = 0 \tag{A4c}$$

In the case of a ring or cylindrical structure, the displacement single-valued condition leads to $B = 0$. Consequently, the stress components are simplified as

$$\sigma_\rho = \frac{A}{\rho^2} + 2C \tag{A5a}$$

$$\sigma_\varphi = -\frac{A}{\rho^2} + 2C \tag{A5b}$$

$$\tau_{\rho\varphi} = \tau_{\varphi\rho} = 0 \tag{A5c}$$

The strain-displacement (geometric) relationship in polar coordinates is given as

$$\begin{cases} \varepsilon_\rho = \dfrac{\partial u_\rho}{\partial \rho} \\ \varepsilon_\varphi = \dfrac{u_\rho}{\rho} + \dfrac{1}{\rho}\dfrac{\partial u_\varphi}{\partial \varphi} \\ \gamma_{\rho\varphi} = \dfrac{1}{\rho}\dfrac{\partial u_\rho}{\partial \varphi} + \dfrac{\partial u_\varphi}{\partial \rho} - \dfrac{u_\varphi}{\rho} \end{cases} \tag{A6}$$

For the elastic plane strain condition, the constitutive equations are formulated as

$$\begin{cases} \varepsilon_\rho = k_1\sigma_\rho + k_2\sigma_\varphi \\ \varepsilon_\varphi = k_1\sigma_\varphi + k_2\sigma_\rho \\ \gamma_{\rho\varphi} = 2\left(k_1 - k_2\right)\tau_{\rho\varphi} \end{cases} \tag{A7}$$

where, k_1 and k_2 can be expressed by are the Young's modulus E and Poisson's ratio υ as $(1-\upsilon^2)/E$ and $-(\upsilon + \upsilon^2)/E$, respectively.

Simultaneously with Eqs. (A5)–(A7), the radial displacement can be determined as

$$u_\rho = \left(k_2 - k_1\right)\frac{A}{\rho} + 2\left(k_1 + k_2\right)C\rho + I\cos\varphi + J\sin\varphi \tag{A8}$$

where, I and J are undetermined constants.

From the mechanical model, it can be seen that the boundary conditions of stress at infinity and at the inner boundary ($\rho = r_0$) of the first lining layer are as follows

$$\sigma_{\rho(n+1)}\big|_{\rho=\infty} = -p \tag{A9a}$$

$$\sigma_{\rho(1)}\big|_{\rho=r_0} = 0 \tag{A9b}$$

where, the subscript $n + 1$ denotes the surrounding geological medium.

At each interface $\rho = r_i\,(i = 1, 2, 3, \ldots, n)$, the continuity of both displacement and stress must be maintained, which can be expressed as follows

$$\sigma_{\rho(i)}\big|_{\rho=r_i} = \sigma_{\rho(i+1)}\big|_{\rho=r_i} \tag{A10a}$$

$$u_{\rho(i)}\big|_{\rho=r_i} = u_{\rho(i+1)}\big|_{\rho=r_i} \tag{A10b}$$

Substituting into Eq. (A9a) gives

$$\sigma_{\rho(n+1)}\big|_{\rho=\infty} = \frac{A_{n+1}}{\rho^2} + 2C_{n+1} = -p \tag{A11}$$

As $\rho \to \infty$, $\dfrac{A_{n+1}}{\rho^2} \to 0$, Eq. (A11) becomes

$$C_{n+1} = -\frac{p}{2} \tag{A12}$$

By substituting Eq. (A5a) into Eqs. (A9b), (A13) can be derived

$$\sigma_{\rho(1)}\big|_{\rho=r_0} = \frac{A_1}{{r_0}^2} + 2C_1 = 0 \tag{A13}$$

By substituting Eq. (A5a) into Eq. (A10a) yields

$$\frac{A_i}{{r_i}^2} + 2C_i - \frac{A_{i+1}}{{r_i}^2} - 2C_{i+1} = 0 \tag{A14}$$

Similarly, Eq. (A8) is substituted into the displacement continuity condition Eq. (A10b), one gets

$$\begin{aligned}&\left(k_{2(i)} - k_{1(i)}\right)\frac{A_i}{r_i} + 2\left(k_{1(i)} + k_{2(i)}\right)C_i r_i + I_i\cos\varphi + J_i\sin\varphi = \\ &\left(k_{2(i+1)} - k_{1(i+1)}\right)\frac{A_{i+1}}{r_i} + 2\left(k_{1(i+1)} + k_{2(i+1)}\right)C_{i+1} r_i + I_{i+1}\cos\varphi + J_{i+1}\sin\varphi\end{aligned} \tag{A15}$$

Eq. (A15) holds for any value of φ. By setting $\varphi = 0, \pi, \pi/2,$ and$3\pi/2$, respectively, the following results can be obtained

$$\begin{cases} I_i = I_{i+1} \\ J_i = J_{i+1} \end{cases} \tag{A16}$$

Rearranging Eq. (A15) yields

$$\left(k_{2(i)} - k_{1(i)}\right)\frac{A_i}{r_i} + 2\left(k_{1(i)} + k_{2(i)}\right)C_i r_i - \left(k_{2(i+1)} - k_{1(i+1)}\right)\frac{A_{i+1}}{r_i} - 2\left(k_{1(i+1)} + k_{2(i+1)}\right)C_{i+1} r_i = 0 \tag{A17}$$

The Eqs. (A12)–(A14) and (A17) given above are necessary for solving the solution for the water intake and outlet tunnel under hydrostatic pressure.

Appendix B

The stress function for the system shown in Fig. 4b,c depends on ρ and φ, which can be given by

$$\Phi = f(\rho)\cos 2\varphi \tag{A18}$$

Upon substitution of Eq. (A18) into the compatibility equation Eq. (A2), one obtains

$$\left[\frac{d^4 f}{d\rho^4} + \frac{2}{\rho}\frac{d^3 f}{d\rho^3} - \frac{9}{\rho^2}\frac{d^2 f}{d\rho^2} + \frac{9}{\rho^3}\frac{df}{d\rho}\right]\cos 2\varphi = 0 \tag{A19}$$

By solving Eq. (A19), we can get

$$f(\rho) = W\rho^4 + F\rho^2 + G + \frac{H}{\rho^2} \tag{A20}$$

where W, F, G, H is the undetermined constant. Eq. (A18) therefore becomes

$$\Phi = \left(W\rho^4 + F\rho^2 + G + \frac{H}{\rho^2}\right) cos2\varphi \tag{A21}$$

The corresponding stress components expressed by the stress function in polar coordinates as follows

$$\begin{cases} \sigma_\rho = -\left(2F + \dfrac{4G}{\rho^2} + \dfrac{6H}{\rho^4}\right)\cos 2\varphi \\ \sigma_\varphi = \left(12W\rho^2 + 2F + \dfrac{6H}{\rho^4}\right)\cos 2\varphi \\ \tau_{\rho\varphi} = \left(6W\rho^2 + 2F - \dfrac{2G}{\rho^2} - \dfrac{6H}{\rho^4}\right)\sin 2\varphi \end{cases} \tag{A22}$$

Combining Eqs. (A6), (A7), and (A22), the radial displacement u_ρ and circumferential displacement u_φ can be obtained as follows

$$u_\rho = -k_1\left(2F\rho - \frac{4G}{\rho} - \frac{2H}{\rho^3}\right)\cos 2\varphi + k_2\left(4W\rho^3 + 2F\rho - \frac{2H}{\rho^3}\right)\cos 2\varphi + H(\varphi) \tag{A23}$$

$$u_\varphi = \frac{k_1}{2}\left(12W\rho^3 + 4F\rho - \frac{4G}{\rho} + \frac{4H}{\rho^3}\right)\sin 2\varphi - \frac{k_2}{2}\left(4W\rho^3 + 4F\rho + \frac{4G}{\rho} + \frac{4H}{\rho^3}\right)\sin 2\varphi - \int H(\varphi)d\varphi + g(\rho) \tag{A24}$$

where, $H(\rho)$ is an arbitrary function of φ, $g(\rho)$ is an arbitrary function of ρ.

Substituting Eqs. (A7), (A22)–(A24) into the third of Eq. (A6), and solved it by separating variables, ones obtained

$$\int H(\varphi)d\varphi + H'(\varphi) = g(\rho) \tag{A25}$$

which has the solution

$$H(\varphi) = I\sin\varphi + J\cos\varphi \tag{A26}$$

where, I and J are undetermined constants.

From Eqs. (A25) and (A26), it can be easily obtained

$$\int H(\varphi)d\varphi = g(\rho) - I\cos\varphi + J\sin\varphi \tag{A27}$$

Taking Eqs. (A26) and (A27) into Eqs. (A23) and (A24), the displacement u_ρ and u_φ given by

$$u_\rho = -k_1\left(2F\rho - \frac{4G}{\rho} - \frac{2H}{\rho^3}\right)\cos 2\varphi + k_2\left(4W\rho^3 + 2F\rho - \frac{2H}{\rho^3}\right)\cos 2\varphi + I\sin\varphi + J\cos\varphi \tag{A28}$$

$$u_\varphi = \frac{k_1}{2}\left(12W\rho^3 + 4F\rho - \frac{4G}{\rho} + \frac{4H}{\rho^3}\right)\sin 2\varphi - \frac{k_2}{2}\left(4W\rho^3 + 4F\rho + \frac{4G}{\rho} + \frac{4H}{\rho^3}\right)\sin 2\varphi + I\cos\varphi - J\sin\varphi \tag{A29}$$

According to the far-field stress boundary conditions as shown in Fig. 4b, we can be obtained

$$\begin{cases} \tau_{\rho\varphi(n+1)}\big|_{\rho=\infty} = \left(6W_{n+1}\rho^2 + 2F_{n+1} - \dfrac{2G_{n+1}}{\rho^2} - \dfrac{6H_{n+1}}{\rho^4}\right)\sin 2\varphi = -\tau\sin 2\varphi \\ \sigma_{\rho(n+1)}\big|_{\rho=\infty} = -\left(2F_{n+1} + \dfrac{4G_{n+1}}{\rho^2} + \dfrac{6H_{n+1}}{\rho^4}\right)\cos 2\varphi = \tau\cos 2\varphi \end{cases} \tag{A30}$$

As $\rho \to \infty$, $1/\rho^2$ and $1/\rho^4$ are tending 0. Therefore, constants W_{n+1} and F_{n+1} given by

$$\begin{cases} W_{n+1} = 0 \\ F_{n+1} = -\frac{\tau}{2} \end{cases} \tag{A31}$$

For the inner boundary of the 1-th lining is free, as illustrated in Fig. 4c, the stress boundary condition can be expressed as

$$\begin{cases} \tau_{\rho\varphi(1)}\big|_{\rho=r_0} = \left(6W_1 r_0^2 + 2F_1 - \dfrac{2G_1}{r_0^2} - \dfrac{6H_1}{r_0^4}\right)\sin 2\varphi = 0 \\ \sigma_{\rho(1)}\big|_{\rho=r_0} = -\left(2F_1 + \dfrac{4G_1}{r_0^2} + \dfrac{6H_1}{r_0^4}\right)\cos 2\varphi = 0 \end{cases} \tag{A32}$$

After simplification, the Eq. (A32) becomes

$$\begin{cases} 6W_1 r_0^2 + 2F_1 - \dfrac{2G_1}{r_0^2} - \dfrac{6H_1}{r_0^4} = 0 \\ 2F_1 + \dfrac{4G_1}{r_0^2} + \dfrac{6H_1}{r_0^4} = 0 \end{cases} \tag{A33}$$

Substituting Eqs. (A28) and (A29) into continuity of displacement condition Eq. (4). After rearrangement, the following equation can be obtained

$$\begin{cases} -k_{1(i)}\left(2F_i r_i - \frac{4G_i}{r_i} - \frac{2H_i}{r_i^3}\right)\cos 2\varphi + k_{2(i)}\left(4W_i r_i^3 + 2F_i r_i - \frac{2H_i}{r_i^3}\right)\cos 2\varphi + I_i \sin\varphi + J_i \cos\varphi = \\ -k_{1(i+1)}\left(2F_{i+1} r_i - \frac{4G_{i+1}}{r_i} - \frac{2H_{i+1}}{r_i^3}\right)\cos 2\varphi + k_{2(i+1)}\left(4W_{i+1} r_i^3 + 2F_{i+1} r_i - \frac{2H_{i+1}}{r_i^3}\right)\cos 2\varphi + I_{i+1}\sin\varphi + J_{i+1}\cos\varphi \\ \frac{k_{1(i)}}{2}\left(12W_i r_i^3 + 4F_i r_i - \frac{4G_i}{r_i} + \frac{4H_i}{r_i^3}\right)\sin 2\varphi - \frac{k_{2(i)}}{2}\left(4W_i r_i^3 + 4F_i r_i + \frac{4G_i}{r_i} + \frac{4H_i}{r_i^3}\right)\sin 2\varphi \\ -q_i \sin 2\varphi / K_i + I_i \cos\varphi - J_i \sin\varphi \\ = \frac{k_{1(i+1)}}{2}\left(12W_{i+1} r_i^3 + 4F_{i+1} r_i - \frac{4G_{i+1}}{r_i} + \frac{4H_{i+1}}{r_i^3}\right)\sin 2\varphi - \frac{k_{2(i+1)}}{2}\left(4W_{i+1} r_i^3 + 4F_{i+1} r_i + \frac{4G_{i+1}}{r_i} + \frac{4H_{i+1}}{r_i^3}\right)\sin 2\varphi \\ + I_{i+1}\cos\varphi - J_{i+1}\sin\varphi \end{cases} \tag{A34}$$

Eq. (A34) is true for any φ, let's set φ to 0 and $\pi/4$. Doing this yields

$$\begin{cases} I_i = I_{i+1} \\ J_i = J_{i+1} \end{cases} \tag{A35}$$

Moreover, at the interface $\rho = r_i$, interface contact stress $q_i \sin 2\varphi$ given by

$$q_i \sin 2\varphi = -\tau_{\rho\varphi(i)} = -\left(6W_i r_i^2 + 2F_i - \frac{2G_i}{r_i^2} - \frac{6H_i}{r_i^4}\right)\sin 2\varphi \tag{A36}$$

Therefore, Eq. (A34) becomes

$$\begin{cases} 4k_{2(i)} r_i^3 W_i - 2\left(k_{1(i)} - k_{2(i)}\right) r_i F_i + \frac{4k_{1(i)}}{r_i} G_i + 2\frac{k_{1(i)} - k_{2(i)}}{r_i^3} H_i - 4k_{2(i+1)} r_i^3 W_{i+1} \\ + 2\left(k_{1(i+1)} - k_{2(i+1)}\right) r_i F_{i+1} - \frac{4k_{1(i+1)}}{r_i} G_{i+1} - 2\frac{k_{1(i+1)} - k_{2(i+1)}}{r_i^3} H_{i+1} = 0 \\ \left[\left(6k_{1(i)} - 2k_{2(i)}\right) r_i^3 + 6r_i^2/K_i\right] W_i + \left[2\left(k_{1(i)} - k_{2(i)}\right) r_i + 2/K_i\right] F_i - \left[2\frac{k_{1(i)} + k_{2(i)}}{r_i} + \frac{2}{r_i^2 K_i}\right] G_i \\ + \left[2\frac{k_{1(i)} - k_{2(i)}}{r_i^3} - \frac{6}{r_i^4 K_i}\right] H_i - \left(6k_{1(i+1)} - 2k_{2(i+1)}\right) r_i^3 W_{i+1} - 2\left(k_{1(i+1)} - k_{2(i+1)}\right) r_i F_{i+1} + \\ 2\frac{k_{1(i+1)} + k_{2(i+1)}}{r_i} G_{i+1} - 2\frac{k_{1(i+1)} - k_{2(i+1)}}{r_i^3} H_{i+1} = 0 \end{cases} \tag{A37}$$

Substitute Eq. (A22) into stress continuity condition Eq. (5), one gets

$$\begin{cases} 6W_i r_i^2 + 2F_i - \frac{2G_i}{r_i^2} - \frac{6H_i}{r_i^4} - 6W_{i+1} r_i^2 - 2F_{i+1} + \frac{2G_{i+1}}{r_i^2} + \frac{6H_{i+1}}{r_i^4} = 0 \\ 2F_i + \frac{4G_i}{r_i^2} + \frac{6H_i}{r_i^4} - 2F_{i+1} - \frac{4G_{i+1}}{r_i^2} - \frac{6H_{i+1}}{r_i^4} = 0 \end{cases} \tag{A38}$$

The Eqs. (A31), (A33), (A37) and (A38) given above are necessary for solving the analytical solution for the composite tunnel under pure shear stress.